Time-reassigned synchrosqueezing transform: The algorithm and its applications in mechanical signal processing

Dong He [a], Hongrui Cao [a,*], Shibin Wang [a], Xuefeng Chen [b]

[a] Xi'anJiaotong University, School of Mechanical Engineering, Xi'an, Shaanxi 710049, PR China
[b] Xi'anJiaotong University, State Key Laboratory for Manufacturing Systems Engineering, Xi'an, Shaanxi 710049, PR China

ARTICLE INFO

ABSTRACT

Synchrosqueezing transform (SST) is an effective post-processing time-frequency analysis (TFA) method in mechanical signal processing. It improves the concentration of the time-frequency (TF) representation of non-stationary signals composed of multiple components with slow varying instantaneous frequency (IF). However, for components whose TF ridge curves are fast varying, or even nearly parallel with frequency axis, the SST still suffers from TF blurs. In this paper, we introduce a TFA method called time-reassigned synchrosqueezing transform (TSST) that achieves highly concentrated TFR for impulsive-like signal whose TF ridge curves is nearly parallel with frequency axis. Moreover, the TSST enables signal reconstruction, compared with the standard TF reassignment methods, such as reassigned short-time Fourier transform and reassigned wavelet transform. In the algorithm of TSST, the group delay estimator is calculated rather than the IF estimator. Furthermore, the TF coefficients are reassigned in the time direction rather than in frequency direction as the SST did. Then we compare the concentration between SST and TSST at different length of Gaussian window and chirp-rate, which is followed by the respective application scope of SST and TSST. Furthermore, we describe an efficient numerical algorithm for practical implementation of TSST. It is found that the SST is suitable for characterizing signal with small chirp-rate while TSST performs better for a large chirp-rate condition. Thus, the TSST is more capable of extracting transient features of impulsive-like signal. Finally, the effectiveness of the TSST and its inverse transform is verified by simulation and experimental studies.

© 2018 Elsevier Ltd. All rights reserved.

1. Introduction

Mechanical fault diagnosis methods under non-stationary operating conditions play a significant role in machinery safe maintenance. The non-stationary operating conditions are easily caused by time-varying load [1], operating speed [2] and transient phenomena [3], which makes it much more difficult to extract fault features from such complex vibration signals [4]. For instance, frequency-based methods like spectral analysis are not suitable for non-stationary conditions as speed fluctuations in rotary machines will smear the spectrum, resulting in a challenge for interpretation from the spectrum for fault feature extraction and the modeling of the control strategy. Therefore, signal processing, feature extraction, and control methods under non-stationary conditions of machines are crucial technologies for health monitoring and fault diagnosis [5,6]. This paper presents an algorithm and its applications for mechanical signal processing under non-stationary operating conditions.

---

* Corresponding author.
  E-mail address: chr@mail.xjtu.edu.cn (H. Cao).

As is known, non-stationary operating conditions make the components of the vibration signal with the time-varying instantaneous frequency (IF) and instantaneous amplitude (IA). Time-frequency analysis (TFA) method is one of the most effective tools for characterizing these time-varying features. Traditional TFA methods can be roughly classified into linear TFAs and quadratic TFAs, but they have respective shortcomings. In linear TFAs, such as short-time Fourier transform (STFT) [7] and continuous wavelet transform (CWT) [5], time-frequency concentration is limited by the Heisenberg uncertainty principle; in quadratic TFAs, such as Wigner-Ville distribution (WVD) [8], good time-frequency resolution can be obtained but interference terms are introduced for multi-component signals, reducing the readability of the time-frequency representation (TFR).

Some researchers proposed various method to sharp the concentration of TFR. Auger and Flandrin proposed a time-frequency post-processing method called time-frequency (time-scale) reassignment method to improve the energy concentration [9]. This kind of standard time-frequency reassignment method (STFRM) includes reassigned short-time Fourier transform (RSTFT) and reassigned wavelet transform (RWT). The STFRM transferred the time-frequency (time-scale) coefficients from the original position to the center of gravity of signal's energy distribution, both along the time axis and the frequency (scale) axis. However, the signal cannot be reconstructed using STFRM [10]. In many application fields, the reconstruction property is precisely a key requirement of the time-frequency analysis method. In order to overcome these shortages, Daubechies et al. [11] proposed a wavelet-based time-frequency post-processing method the called synchrosqueezing wavelet transform (SWT), which is a special case of the STFRM. The advantages of SWT consist of two aspects: one is allowing reconstruction to the time domain, just like empirical mode decomposition (EMD) [12], and the other is computational efficiency superior to RWT in that SWT is one-dimensional integrals while RWT is two-dimensional integrals.

Because of these advantages, the SWT is widely studied in theory and application. SWT was then extended to STFT based synchrosqueezing transform (SFT) [13]. Both SWT and SFT belong to synchrosqueezing transform (SST) family. Further, the stability properties of the SWT were analyzed and its robustness to bounded perturbations of the signal was demonstrated [14]. Later on, Li et al. [15,16] proposed a generalized synchrosqueezing transform to reduce the diffusions in both time and frequency dimensions. Feng et al. [17] proposed iterative generalized synchrosqueezing transform to improve the readability of TFR. Xi et al. [18] proposed a frequency-shift synchrosqueezing method which shifted the high-frequency component to the low-frequency zone to improve the instantaneous frequency (IF) estimation accuracy of high-frequency components. Wang et al. proposed a matching demodulation transform and then employed SFT technology to enhance the TF energy concentration for strong frequency modulated signals [19]. Wang further proposed CWT-based and STFT-based matching synchrosqueezing transform (MSST) which introduced chirp rate estimation into a comprehensive IF estimation to match the TF structure of the signals with fast varying IF [20,21]. Cao and Xi et al. [22,23] proposed zoom synchrosqueezing transform (ZST) based on the SWT, where the signal was frequency shifted and synchrosqueezed in a specific frequency region. Moreover, SST has studied and applied in a wide range of field, such as paleoclimate applications [14], geography [24,25], finance [26], medicine [27–29], vibration analysis [22,30,31], structural health monitoring [32], modal identification [33,34] and machining chatter detection [35,36].

However, SST also has some limits. It should be noted that the signals analyzed by SST are modeled by intrinsic mode functions (IMF) [11]:

$$x(t) = \sum_{k=1}^{K} A_k(t)e^{i\phi_k(t)} \tag{1}$$

where $A_k(t)$ and $\phi_k(t)$ are the IA and instantaneous phase of the kth amplitude modulated–frequency modulated (AM–FM) component of the signal, respectively. The SST will obtain high concentrated TFR and accurate invertible properties if the change rate of $A_k(t)$ and $\phi'_k(t)$ is much slower than the change rate of $\phi_k(t)$ itself [11]. This means that the individual components of $x(t)$ can be locally approximated as a harmonic signal. However, it is not precise to locally approximate signals with fast varying IF as harmonic signals because their energy in TF domain distributed along both time and frequency directions. The TFR of signals with fast varying IF will get blurred since SST only reassigns the TF energy in the scale/frequency direction and ignores the time direction [15]. Theoretical analysis has shown that the estimation error of IF estimator and the reconstruction error increases by the change rate of $A_k(t)$ and $\phi'_k(t)$ [11]. The STFRM reassigns the TF energy both along the time and the frequency/scale axis, but it is no longer invertible and does not allow for mode reconstruction [10]. In order to cope with the contradiction between concentration and reconstruction property, Wang et al. proposed MSST and defined a class of chirp-like intrinsic-mode functions (CIMF) [20,21]. The standard SST requires $|\phi''_k(t)| < \varepsilon$, while this restriction is relaxed in MSST as $|\phi''_k(t)| < \infty$, so MSST has the wider scope of application and better ability to characterize the signals with fast varying IF than the harmonic-like IMF model in [11]. However, it is difficult to approximate the IF where the change rate of chirp-rate $|\phi'''_k(t)|$ is very high (nearly impulsive signal). In order to increase the approximation order, Pham et al. proposed high-order synchrosqueezing transform where the comprehensive IF estimator was computed more accurately by a higher order partial derivative of STFT [37]. Pham's study dealt with a wide variety of multicomponent signals containing very strongly modulated AM-FM modes and can retrieve modes with high accuracy.

It can be found that the original SST and its improvement methods mostly reassign the TF energy in the scale/frequency direction and they are suitable for characterizing harmonic-like signals, which display like horizontal lines in the TFR. As shown in Fig. 1(a), each time instant u corresponds to only one frequency point ξ for each component. Apart from the harmonic-like signals, the other kind of non-stationary signals could be termed as impulsive-like signals, which are
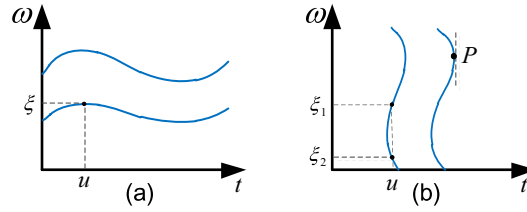
Fig. 1. Time-frequency structure of (a) harmonic-like signal and (b) impulsive-like signal (the blue curves are time-frequency ridges). (For interpretation of the references to colour in this figure legend, the reader is referred to the web version of this article.)

investigated extensively in many fields, for example, delta function $\delta(t)$ or other transient signals localized at small support set in time domain. The TFRs of these signals display like vertical lines in the TFR and some certain time instant u corresponds to NOT only one frequency point ξ for each component. As shown in Fig. 1(b), the tangent at point P is perpendicular to the time axis, so $|\phi''_k(t)| \to \infty$ on this particular time-frequency points. The condition $|\phi''_k(t)| < \infty$ in MSST does not hold anymore, so the TFR will get blurred at point P. Therefore, the reassignment direction should be modified before it is used for impulsive-like signals. Moreover, for impulsive-like signals, the high-order derivatives of IF are likely so large that MSST cannot approximate the IF properly. While the high-order synchrosqueezing transform in Ref. [37] could obtain satisfactory TFR, it requires high order parameters for approximation and is sometimes complex for computation. Additionally, for the second or high order synchrosqueezing transform, one should consider the condition where the denominator of the ratio of STFTs respect to window function's higher derivative is very small. If the threshold of these STFTs is not set properly, some important TF information will be missed. Therefore, it is necessary to achieve low order approximation but to obtain nearly the same result as high-order synchrosqueezing transform for practical efficient computation. In order to improve the accuracy of time-frequency analysis and reconstruction, the original SST needs to be modified to extract the transient feature in impulsive-like signals accurately.

As mentioned above, for impulsive-like signals, time-frequency reassignment method considers the time and frequency/scale variables simultaneously to obtain a high concentrated TFR, but it is not invertible for signal reconstruction and has lower computation efficiency. The original SST methods only reassign the TF energy in the scale/frequency direction. However, for analysis of impulsive-like signals, the errors of candidate IF and reconstruction will increase, resulting in a blurred TFR and inaccurate separated components. In this paper, a modified version of SST is proposed to achieve a relatively highly concentrated TFR for impulsive-like signals. More importantly, the proposed method allows for reconstruction of each component like the standard SST and the computation complexity remains the same. The key contribution is that the reassignment operation is implemented in the time direction, rather than scale/frequency direction as the SST did. The IF estimator in reassignment operation is replaced by group delay (GD) estimator. Since the reassignment direction is time direction, the modified SST is called time-reassigned synchrosqueezing transform (TSST). In this sense, the TSST is a complementary method to SST. In addition, both SST and TSST can be viewed as special cases of STFRM enabling mode reconstruction, as shown in Fig. 2. In the TSST method, a strong time-varying signal in time-domain becomes weak *frequency-varying* in the frequency domain. Therefore, for impulsive-like signals, a high-order approximation can be transformed into low-order approximation, which can be easier to accomplish. In this paper, TSST is studied in the STFT framework but it can be extended to WT framework easily since they are the similar linear method. Moreover, we later describe an efficient
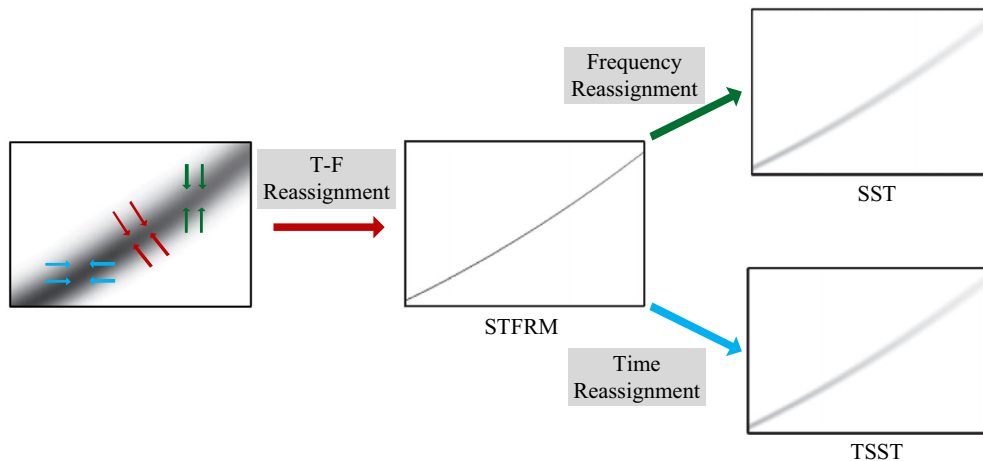

Fig. 2. Comparison among SST and TSST and STFRM. The reassignment is performed along frequency direction, time direction and both, respectively.

numerical algorithm for the practical implementation of the TSST. Another important contribution of the paper is to provide the reconstruction strategy for the TSST generated for impulsive-like signals. In this process, a refined GD extraction method designed for the TSST is presented to retrieve individual components of the synthetic signal for reconstruction using time-frequency filtering and reconstruction from TFR with less computing burden.

The remainder of this paper is organized as follows. In Section 2, the TF reassignment method and the STFT-based SST are reviewed. In Section 3, the definition and property of TSST are given and its practical implementation is described in a discrete form. In Section 4, the SST and TSST are compared, which is followed by the respective application scope and parameter selection strategy. In Section 5, the concentration, robustness, and invertibility of TSST are verified by the Lamb wave simulation. Then the TSST is tested on a Bently test rig and is applied to rub-impact fault diagnosis of an air compressor. The discussion is given in Section 6. Finally, conclusions are drawn in Section 7.

2. Theoretical basis

2.1. Short-time Fourier transform and reassigned spectrogram

The modified STFT can be regarded as the inner product of $x(t)$ and a short-time Fourier atom $g(t-u)e^{i\xi(t-u)}$, which is constructed with a window function $g(t)$ modulated by the frequency ξ and translated by u:

$$S_x^g(u,\xi) = \langle x(t), g(t-u)e^{i\xi(t-u)}\rangle = \int x(t)g(t-u)e^{-i\xi(t-u)}\mathrm{d}t = M_x^g(u,\xi)e^{i\Phi_x^g(u,\xi)} \tag{2}$$

where $M_x^g(u,\xi)$ and $\Phi_x^g(u,\xi)$ denotes its magnitude and its phase, respectively. Then the spectrogram is the squared modulus of the STFT, i.e., $P_x^g(u,\xi) = |S_x^g(u,\xi)|^2$. The spectrogram can be further described by Plancherel's theorem as

$$\begin{aligned}
P_x^g(u,\xi) &= \left|S_x^g(u,\xi)\right|^2 = S_x^g(u,\xi) \cdot \overline{S_x^g(u,\xi)} \\
&= \frac{1}{2\pi}\int x(t)g(t-u)e^{-i\xi(t-u)}\mathrm{d}t \cdot \int \hat{x}(\omega)\hat{g}(\omega-\xi)e^{i\omega u}\mathrm{d}\omega \\
&= \iint \frac{1}{2\pi}x(t)g(t-u)\hat{x}(\omega)\hat{g}(\overline{\omega}-\xi)e^{-i\xi(t-u)}e^{-i\omega u}\mathrm{d}t\mathrm{d}\omega \\
&= \iint Q_{u,\xi}(t,\omega)\mathrm{d}t\mathrm{d}\omega
\end{aligned} \tag{3}$$

where $Q_{u,\xi}(t,\omega) = \frac{1}{2\pi}x(t)g(t-u)\hat{x}(\omega)\hat{g}(\overline{\omega}-\xi)e^{-i\xi(t-u)}e^{-i\omega u}$ and it can be regarded as the probability distribution function around TF point (u,ξ). Thus, combined with Eq. (2), the center of gravity of signal's energy distribution around TF point (u,ξ) is

$$\begin{aligned}
\hat{\omega}_x(u,\xi) &= \frac{\iint \omega \cdot Q_{u,\xi}(t,\omega)\mathrm{d}t\mathrm{d}\omega}{\iint Q_{u,\xi}(t,\omega)\mathrm{d}t\mathrm{d}\omega} = \partial_u \Phi_x^g(u,\xi) + i\frac{\partial_u M_x^g(u,\xi)}{M_x^g(u,\xi)} \\
\hat{t}_x(u,\xi) &= \frac{\iint t \cdot Q_{u,\xi}(t,\omega)\mathrm{d}t\mathrm{d}\omega}{\iint Q_{u,\xi}(t,\omega)\mathrm{d}t\mathrm{d}\omega} = u - \partial_\xi \Phi_x^g(u,\xi) + i\frac{\partial_\xi M_x^g(u,\xi)}{M_x^g(u,\xi)}
\end{aligned} \tag{4}$$

The detailed derivation process is available in Appendix A. The real parts of $\hat{\omega}_x(u,\xi)$ and $\hat{t}_x(u,\xi)$ only involve the phase of the complex TFR $S_x^g(u,\xi)$. We can get the definition of so-called reassignment operators for RSTFT as follows:

$$\begin{aligned}
\hat{\omega}_x(u,\xi) &= \partial_u \Phi_x^g(u,\xi), \\
\hat{t}_x(u,\xi) &= u - \partial_\xi \Phi_x^g(u,\xi)
\end{aligned} \tag{5}$$

The frequency reassignment operator and the time reassignment operator are also termed channelized instantaneous frequency and local group delay, respectively [38]. The frequency reassignment operator and the time reassignment operator are both the partial derivatives of the phase of STFT and they can be further described as

$$\begin{aligned}
\hat{\omega}_x(u,\xi) &= \partial_u \Phi_x^g(u,\xi) = \Im\left[\frac{\partial_u S_x^g(u,\xi)}{S_x^g(u,\xi)}\right] \\
\hat{t}_x(u,\xi) &= u - \partial_\xi \Phi_x^g(u,\xi) = u - \Im\left[\frac{\partial_\xi S_x^g(u,\xi)}{S_x^g(u,\xi)}\right]
\end{aligned} \tag{6}$$

where $\Im[\cdot]$ is the imaginary part of complex number. The aim of the RSTFT is to move the value of each TF point from the point of computation to the center of gravity $(\hat{t}_x(u,\xi), \hat{\omega}_x(u,\xi))$.

$$RSP_x^g(u,\xi) = \frac{1}{2\pi}\int\int P_x^g(t,\omega)\delta(t,\omega)\delta(t-\hat{t}_x(u,\xi))\delta(\omega-\hat{\omega}_x(u,\xi))\mathrm{d}u\mathrm{d}\xi \tag{7}$$

Compared with traditional TFR, the RSTFT can greatly improve the energy concentration. However, the signal cannot be reconstructed owing to the RSTFT reassigns the TF energy both along the time and the frequency axis, which limits its applications.

2.2. STFT-based synchrosqueezing transform

Daubechies et al. proposed a post-processing method of TFR called WT-based SST [11], which provides an alternative theoretical way to understand the principle of EMD [12]. WT-based SST is similar with EMD for it can characterize components with time-varying spectrum clearly, and more importantly, it allows retrieval of each component. The reassignment procedure is then applied to other linear TFA methods like STFT [13]. The proposed method in Section 3 is also based on STFT. For comparison, we review the definition and the main theorem for the STFT-based SST in this subsection.

The STFT-based SST is performed via three successive steps. The first step is the calculation of the STFT representation $S_x^g(u,\xi)$ of the analyzed signal $x(t)$ by Eq. (2). The second step is to calculate the IF estimator $\hat{\omega}_x(u,\xi)$ for the signal as follows:

$$\hat{\omega}_x(u,\xi) = \begin{cases} |\Im[\partial_u S_x^g(u,\xi)/S_x^g(u,\xi)]|, & |S_x^g(u,\xi)| > \gamma \\ \infty & |S_x^g(u,\xi)| \leqslant \gamma \end{cases} \tag{8}$$

where γ denotes the threshold. The final step is to reallocate the TF energy from the computational position to the center of gravity in the frequency direction, which transforms the information from the (u,ξ) plane to the $(u,\hat{\omega}_x(u,\xi))$ plane:

$$T_x(u,\omega) = \int_{\Xi_{x,S(u)}} S_x^g(u,\xi)\delta(\omega - \hat{\omega}_x(u,\xi))\mathrm{d}\xi \tag{9}$$

The discrete form of Eq. (9) is

$$T_x(u,\omega_l) = \sum_{k:|\hat{\omega}_x(u,\xi_k)-\omega_l|\leqslant\Delta\omega/2} S_x^g(u,\xi)(\Delta\xi) \tag{10}$$

As thus, the synchrosqueezing operation in improve the TF concentration of STFT. In addition to a sharper TFR, the other advantage of SST superior to RSTFT is invertibility. The inverse transform of SST is based on the inverse transform of STFT. According to Eq. (2) and Plancherel's theorem we have

$$S_x^g(u,\xi) = \frac{1}{2\pi}\int \hat{x}(\omega)\hat{g}(\omega - \xi)e^{i\omega u}\mathrm{d}\omega \tag{11}$$

Integrate $S_x(u,\xi)$ along frequency axis and we obtain

$$\begin{aligned} \int S_x^g(u,\xi)\mathrm{d}\xi &= \frac{1}{2\pi}\iint \hat{x}(\omega)\hat{g}(\omega - \xi)e^{i\omega u}\mathrm{d}\xi\mathrm{d}\omega \\ &= \int\left[\frac{1}{2\pi}\int \hat{g}(\omega - \xi)\mathrm{d}\xi\right]\hat{x}(\omega)e^{i\omega u}\mathrm{d}\omega \\ &= 2\pi g(0)\int \hat{x}(\omega)e^{i\omega u}\mathrm{d}\omega \\ &= 2\pi g(0)x(u) \end{aligned} \tag{12}$$

Thus, we obtain

$$x(u) = \frac{1}{2\pi g(0)}\int S_x^g(u,\xi)\mathrm{d}\xi \tag{13}$$

Like the inverse STFT, the inverse transform of STFT-based SST can be described as the sum of each column of the TF matrix $T_x(u,\omega_l)$

$$x(u) = \frac{1}{2\pi g(0)}\Re\left\{\sum_l T_x(u,\omega_l)\right\} \tag{14}$$

where $\Re[\cdot]$ is the real part of complex number. The STFT-based SST can get reasonable accuracy for slowly time-varying FM signals [13]. This kind of signals is depicted as a set of all superposition of well-separated IMFs in Eq. (1). For each time t, the instantaneous amplitude $A_k(t)$ and instantaneous phase $\phi_k(t)$ of each element of $x_k(t)$ should satisfy $|A'_k(t)| < \varepsilon|\phi'_k(t)|$ and $|\phi''_k(t)| < \varepsilon$, where ε is sufficiently small and the superscript denotes the derivative respect to time. It should be noted that the condition $|\phi''_k(t)| < \varepsilon$ is so strict that it is only suitable for slowly time-varying FM signals. However, for strong time-varying or even impulsive-like signals, the chirp-rate is relatively large, resulting the condition $|\phi''_k(t)| < \varepsilon$ does not hold anymore. Thus, some TFA methods designed for strong time-varying or even impulsive-like signals need to be proposed.

3. Time-reassigned synchrosqueezing transform

3.1. The definition of time-reassigned synchrosqueezing transform

In this section, TSST is proposed to improve the energy concentration of the TF representation for impulsive-like signals. The TSST can assign TFR in the time direction and preserve the invertible properties. In this paper, TSST is based on STFT but it can be extended to WT easily. For convenience, different from Section 2, the STFT in the TSST framework is described as

$$S_x^g(u, \xi) = \int x(t)g(t-u)e^{-i\xi t}dt = \frac{1}{2\pi} \int \hat{x}(\omega)\hat{g}(\omega - \xi)e^{i(\omega - \xi)u}d\omega \tag{15}$$

To motivate the idea, an impulse signal $x_\delta(t)=A\delta(t-t_0)$ is considered as an example. The STFT of $x_\delta(t)$ with the real symmetric window $g_\xi(t)$ is

$$S_{x_\delta}^g(u, \xi) = A \int \delta(t - t_0)g(t - u)e^{-i\xi t}dt = Ag(t_0 - u)e^{-i\xi t_0} \tag{16}$$

Then we have

$$\partial_\xi S_{x_\delta}^g(u, \xi) = -it_0 \cdot S_{x_\delta}^g(u, \xi) \tag{17}$$

which follows that $t_0 = i\partial_\xi S_{x_\delta}^g(u, \xi)/S_{x_\delta}^g(u, \xi)$. Thus, in TSST, the GD estimator of an impulse signal $x_\delta(t)$ is defined as

$$\hat{t}_x(u, \xi) = -\frac{\partial_\xi S_{x_\delta}^g(u, \xi)}{iS_{x_\delta}^g(u, \xi)} = t_0 \tag{18}$$

It should be noted that Eq. (18) is different from Eq. (5) in two aspects. Firstly, u is omitted since we have multiplied a phase modulation term $e^{-i\xi u}$ to change the form of $S_x^g(u, \xi)$:

$$S_x^g(u, \xi) \cdot e^{-i\xi u} \rightarrow S_x^g(u, \xi) \tag{19}$$

Secondly, $\Im[\cdot]$ is omitted since the toy signal is impulse signal. Therefore, in TSST, without loss of generality, we define the GD estimator $\hat{t}_x(u, \xi)$ as

$$\hat{t}_x(u, \xi) = -\partial_\xi \Phi_x^g(u, \xi) = -\Im\left[\frac{\partial_\xi S_x^g(u, \xi)}{S_x^g(u, \xi)}\right], \quad |S_x^g(u, \xi)| > \tilde{\varepsilon} \tag{20}$$

The synchrosqueezing operation in TSST is defined in continuous form as

$$V_x(t, \xi) = \int_{\Xi(\xi)} S_x^g(u, \xi)\delta(t - \hat{t}_x(u, \xi))du \tag{21}$$

where $\Xi(\xi) = \left\{u \in \mathbb{R}; |S_x^g(u, \xi)| > \tilde{\varepsilon}\right\}$. It shows that the TSST reassigns the information from the (u, ξ) plane to the $(\hat{t}_x(u, \xi), \xi)$ plane instead of the $(u, \hat{\omega}_x(u, \xi))$ plane in the original SST. The TSST uses the phase information of the STFT to estimate the group delay operator and relocate the TF coefficients near the group delay operator to obtain the exact time instant for the impulsive-like signal.

One of the advantages of TSST over RSTFT is computational efficiency for TSST is one-dimensional integral. More importantly, like original SST, TSST has invertible property. Firstly, we start from inverse STFT

$$
\begin{aligned}
\int S_x^g(u, \xi)du &= \iint x(t)g(t - u)e^{-i\xi t}dtdu \\
&= \int \left[\int g(t - u)du\right]x(t)e^{-i\xi t}dt \\
&= \hat{g}(0)\int x(t)e^{-i\xi t}dt \\
&= \hat{g}(0)\hat{x}(\xi)
\end{aligned}
\tag{22}
$$

Thus we obtain

$$\hat{x}(\xi) = \frac{1}{\hat{g}(0)} \int S_x^g(u, \xi)du \tag{23}$$

which means that the STFT can be reconstructed into the frequency domain by integrating into the time direction. Since the coefficients are also only relocated in the time domain, the reconstruction of TSST is still achievable by summing up the coefficients in the time domain as follows:

$$\hat{x}(\xi) = \frac{1}{\hat{g}(0)} \int V_x(u, \xi)du \tag{24}$$

which has the same form as Eq. (23). After the signal is reconstructed into the frequency domain via inverse TSST, the inverse Fourier transform can be performed later to transform the spectrum into the time domain. Thus, the TSST provides a powerful tool for signal separation and denoising in the time-frequency plane.

The key contribution of the TSST is that the GD estimator is introduced to replace the IF estimator in the original SST. Since the GD estimator can depict the change of GD for each component of signals in the frequency domain, especially when the change-rate of GD is nearly zero, i.e. the change-rate of IF is infinite. In the TSST method, a strong time-varying signal in time-domain becomes weak *frequency-varying* in the frequency domain. Therefore, for impulsive-like signals, a high-order approximation for IF in SST can be replaced by low-order approximation for GD in TSST.

3.2. The properties of the TSST

(1) Ideal TFR for pure impulsive signal $x_\delta(t)$

Considering a pure impulsive signal $x_\delta(t)$, its TSST can be described as

$$V_x(t, \xi) = \int_{\Xi(\xi)} S_x^g(u, \xi)\delta(t - t_0)\mathrm{d}u = \int_{\Xi(\xi)} Ag(t_0 - u)e^{-\mathrm{i}\xi t_0}\delta(t - t_0)\mathrm{d}u$$
$$= Ae^{-\mathrm{i}\xi t_0}g(0)\delta(t - t_0) \tag{25}$$

Then we have

$$|V_x(t, \xi)| = Ag(0)\delta(t - t_0) \tag{26}$$

This property shows that the TSST can obtain the ideal time-frequency distribution of the pure impulsive signal. The time-frequency coefficients only exist at the time of occurrence of the impulsive signal in the time-frequency plane. Moreover, the coefficients only depend on the amplitude of the signal itself. The coefficients are zero on the other part of the time-frequency plane. Among many time-frequency analysis methods, only the WVD and STFRM have the property of ideal time-frequency distribution of the impulse signal, except for TSST. However, neither of these two methods has the reconstruction property.

(2) Time and frequency shift invariance

Suppose a signal $x(t)$ is translated in time by t_0 and translated in frequency by ω_0, which is given by $y(t) = x(t - t_0)e^{\mathrm{i}\omega_0 t}$, the STFT of signal $y(t)$ is

$$S_y(u, \xi) = S_x(u - t_0, \xi - \omega_0)e^{\mathrm{i}\omega_0 u} \tag{27}$$

Thus, we have

$$\hat{\omega}_y(u, \xi) = \hat{\omega}_x(u - t_0, \xi - \omega_0) + \omega_0, \hat{t}_y(u, \xi) = \hat{t}_x(u - t_0, \xi - \omega_0) + t_0, \tag{28}$$

$$V_y(t, \xi) = V_x(t - t_0, \xi - \omega_0)e^{\mathrm{i}\omega_0 u} \tag{29}$$

This property shows that when the signal is time-shifted or frequency-shifted, the IF estimator and the GD estimator will also produce corresponding time shift and frequency shift, respectively. This means the time and frequency shift of the estimator will cause the increase or decrease in time or frequency of movement. The magnitude of the TSST will be time-shifted and frequency-shifted, and its phase function will also produce corresponding frequency shift.

(3) Complex conjugate property

If $x : \mathbb{R} \to \mathbb{C}$ and $y(t) = \overline{x(t)}$, then $S_y(u, \xi) = \overline{S_x(u, -\xi)}$. Thus, we have

$$\hat{\omega}_y(u, \xi) = -\hat{\omega}_x(u, -\xi), \ \hat{t}_y(u, \xi) = \hat{t}_x(u, -\xi) \tag{30}$$

$$V_y(t, \xi) = \overline{V_x(t, -\xi)} \tag{31}$$

(4) Hermitian property

If $x : \mathbb{R} \to \mathbb{R}$, then $S_x(u, -\xi) = \overline{S_x(u, \xi)}$. Thus, we have

$$\hat{\omega}_x(u, \xi) = -\hat{\omega}_x(u, -\xi), \ \hat{t}_x(u, \xi) = \hat{t}_x(u, -\xi) \tag{32}$$

$$V_x(t, -\xi) = \overline{V_x(t, \xi)} \tag{33}$$

This property shows that when the signal is a real signal, the GD estimator is symmetrical around the frequency axis, while the IF estimator is symmetrical around the origin. The magnitude and phase of the TSST are symmetrical around the origin and symmetrical on the frequency axis, respectively.

3.3. The discrete form of TSST

In this section, we present a practical implementation of TSST in a discrete form which is suitable for efficient numerical calculation.

3.3.1. TSST forward transform

The most important step of TSST is to calculate the GD estimator of the signal according to Eq. (20). However, taking differences of $S_x^g(u, \xi)$ respect to ξ directly can be somewhat unstable considering the signal suffered from noise sometimes. In

order to improve the computational stability, an alternative method is derived mathematically. The definition of the TSST in the continuous form is reviewed here, and according to the derivation about $\partial_\xi S_x^g(u, \xi)$ in Eq. (20), we have

$$
\begin{aligned}
\partial_\xi S_x^g(u, \xi) &= \partial_\xi \left[\int x(t) g(t - u) e^{-i\xi t} dt \right] \\
&= \int x(t) g(t - u) \partial_\xi (e^{-i\xi t}) dt \\
&= -i \int t x(t) g(t - u) e^{-i\xi t} dt \\
&= -i S_{tx}^g(u, \xi)
\end{aligned}
\tag{34}
$$

Thus we obtain

$$
\hat{t}_x(u, \xi) = \Re \left[\frac{S_{tx}^g(u, \xi)}{S_x^g(u, \xi)} \right]
\tag{35}
$$

It can be observed that the term $\partial_\xi S_x^g(u, \xi)$ is replaced by $S_{tx}^g(u, \xi)$ for the calculation of the GD estimator. In practice, the observed signal is real-valued and discrete, $x[n]$, $n = 0, 1 \ldots, N - 1$ where N is the number of samples. Its element $x[n]$ corresponds to a uniform discretization of $x(t)$ taken at the time instant $t_n = t_0 + nT$, where T is the sampling interval, and the corresponding sampling frequency is $f_s = 1/T$. Thus, the angular frequency interval is $\triangle \xi = 2\pi/NT$ and the discrete angular frequency is $\xi[k] = k \triangle \xi$, $k = 0, 1 \ldots, N - 1$.

We now describe a fast computation for the TSST. The efficiency of this algorithm lies in three key steps. The first step of the TSST is the calculation of the STFT of the discrete signal $x[n]$ involved in Eq. (35), including $S_x^g(u, \xi)$ and $S_{tx}^g(u, \xi)$. The discrete form for $S_x^g(u, \xi)$ and $S_{tx}^g(u, \xi)$ are written as $S_x^g[n, k]$ and $S_{tx}^g[n, k]$, respectively, $n = 0, 1 \ldots, N - 1$; $k = 0, 1 \ldots, N - 1$. Then we obtain

$$
S_x^g[n, k] = \sum_{j=0}^{N-1} x[j] \cdot g[j - n] \cdot e^{-2\pi jk/N}
\tag{36}
$$

$$
S_{tx}^g[n, k] = \sum_{j=0}^{N-1} t[j] \cdot x[j] \cdot g[j - n] \cdot e^{-i2\pi jk/N}
\tag{37}
$$

where $g[\cdot]$ denotes the N-point window function. Let F_N be the standard discrete Fourier Transform. Then we have

$$
S_x^g[n, \cdot] = F_N(x_n \odot g)
\tag{38}
$$

$$
S_{tx}^g[n, \cdot] = F_N(t_n x_n \odot g)
\tag{39}
$$

where $\odot$ denotes element-wise multiplication. This procedure can be implemented using fast Fourier transform (FFT).

The second step of the TSST is the calculation of the GD estimator. For numerical stability, a support zone for the $S_x^g[n, k]$ is defined as

$$
S_y[k] = \left\{ n : |S_x^g[n, k]| > \gamma \right\}, \quad for \quad k = 0, 1 \ldots, N - 1;
\tag{40}
$$

where γ is the threshold to overcome the unstable phenomenon (usually set as 10^{-8}). Then, the GD estimator of discrete form for the discrete signal $x[n]$ is calculated, for $k \in \mathcal{S}_\gamma[n]$, as

$$
\hat{t}_x[n, k] = \Re \left\{ \frac{S_{tx}^g[n, k]}{S_x^g[n, k]} \right\}
\tag{41}
$$

This discrete GD estimator contains the GD information of the discrete signal, which allows us to transfer from the TF plane to a frequency-GD plane.

The last step of the TSST is the synchrosqueezing process in the TF plane. For the discrete signal $x[n]$, this synchrosqueezing is realized by summing different contributions from their original position to where the GD estimator points.

$$
V_x[m, k] = \sum_{n: |\hat{t}_x[n, k] - t[m]| \leqslant T/2} S_x^g[n, k]
\tag{42}
$$

The diagram for the practical implementation for the TSST is shown in Fig. 3.

3.3.2. TSST reconstruction

The main advantage of the TSST over RSTFT methods is its invertibility. Not only does the TSST improve the energy concentration of the TF representation for impulsive-like signal, but also it enables signal reconstruction in a convenient mathematical framework.

Let $m \in \mathcal{M}_n[k]$ be the indices of the zone around the GD of the component x_k. Then, the reconstruction can be implemented by adding up TF coefficients in $\mathcal{M}_n[k]$ for each row of the time-frequency matrix $V_x[m, k]$
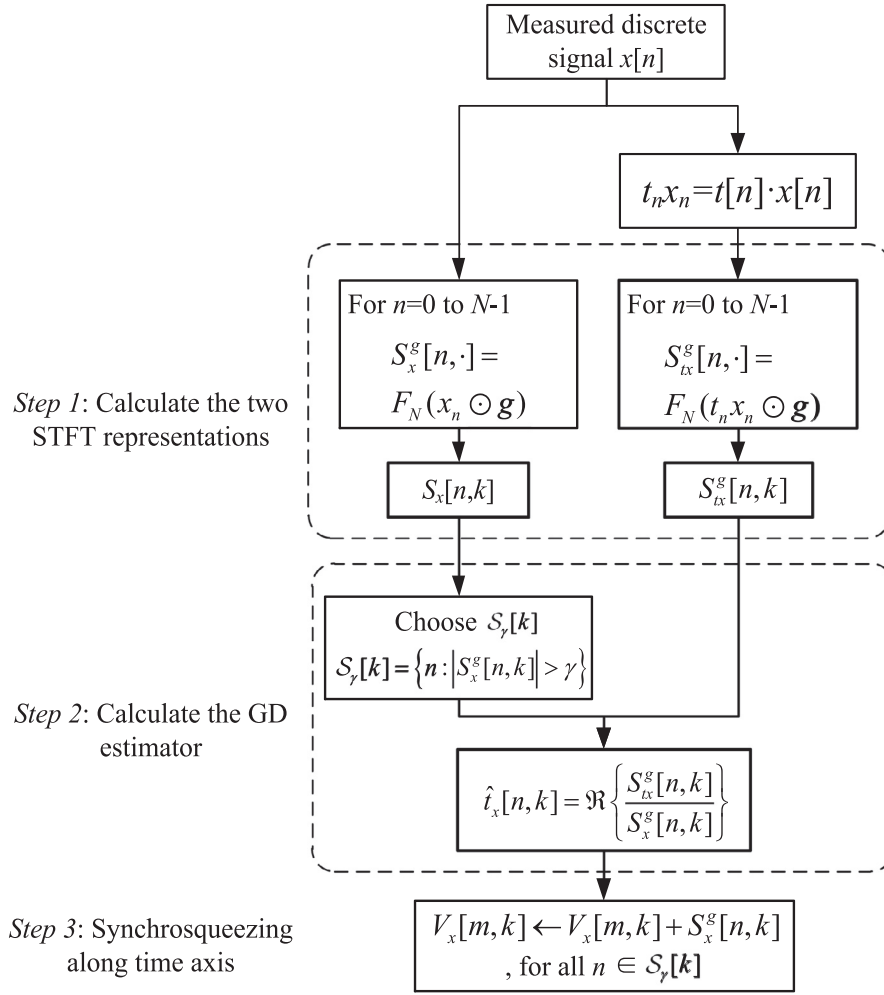
Fig. 3. The diagram of the implementation for TSST.

$$\hat{x}[k] = \frac{1}{\hat{g}(0)} \sum_{m \in \mathcal{M}_n[k]} V_x[m, k] \qquad (43)$$

where $\hat{x}[\cdot]$ is complex value because it is the complex spectrum of the signal $x[n]$. The time-domain signal can also be calculated through inverse DFT of $\hat{x}[k]$:

$$x_r[n] = \frac{1}{N} \sum_{k=0}^{N-1} \hat{x}[k] \cdot e^{i2\pi nk/N} \qquad (44)$$

The most crucial step for the implementation of the TSST reconstruction is the GD curves extraction. In this study, we use an alternative approach for GD estimation based on a ridge detection algorithm called Viterbi algorithm [8], in which both the maximum energy in the local area of the TSST representation and the smooth of the curve are considered. The curves extraction method is initially designed for extracting IF from TFRs of harmonic-like signals. Thus, it is hard to extract "vertical" GD curves of an impulsive signal using Viterbi algorithm directly. Fortunately, after rotating TFR by 90 degrees, the Viterbi algorithm can be implemented to extract relatively "horizontal" GD curves. In the Viterbi algorithm, a cost function is introduced to balance the effect of the local maximum and the smooth of the curve. The starting point for searching is estimated by maximum magnitude of the TFR, and the successive TF point on the expectant TF ridge can be extracted step by step via dynamically minimizing the local cost functions. After finding the first component, one sets $V_x[m, k]$ for $m \in \mathcal{M}_n[k]$ $k = 0, 1, \ldots, N - 1$ to zero and repeat the aforementioned ridge extraction procedure on the remaining TSST representation. Therefore, this ridge detection algorithm can effectively extract ridges of each component from the TSST representation to estimate respective GD.

4. Comparative study

In this section, the comparison results of the STFT, the SST and the TSST are illustrated via some simulation examples. Firstly, we use a toy signal to illustrate the property of the TSST towards the ideal TFR of impulsive-like signal $x(t)$

$$x(t) = (\pi\sigma^2)^{-1/4}\exp\left[-(t-t_0)^2/2\sigma^2\right] \tag{45}$$

where $\sigma = 1 \times 10^{-5}$, which denotes the standard deviation of the Gaussian function; $t_0 = 0.5$, which is the time of occurrence of the impulsive signal. The sampling frequency is 1024 Hz.

Fig. 4 gives the comparison result of the STFT, the SST, and the TSST of the simulation example. It can be observed that the TSST can squeeze the STFT to an almost ideal representation of the toy signal in the time-frequency space. In contrast, the SST provides no improvement from STFT. This is because TSST relocates TF coefficients along the time axis, just the same as the disperse direction of the impulsive signal while SST relocates TF coefficients along frequency axis on which the energy is constant.

In order to generalize the simulation, we consider a Gaussian chirp time-frequency atom, which is described as

$$x(t) = \exp\left\{\frac{(t-t_0)^2}{2\sigma_0^2} + i2\pi\left[f_0(t-t_0) + \frac{1}{2}c(t-t_0)^2\right]\right\} \tag{46}$$

The signal parameters and analytical parameters are listed in Table 1. For comparing the performance of SST and TSST quantitatively at different chirp rates, the Rényi entropy [39,40] is used to evaluate the energy concentration of the TFR obtained by different TFA methods. The Rényi entropy of order α for a TFR $P(u,\xi)$ is defined as

$$R_P^\alpha = \frac{1}{1-\alpha}\log_2 \iint \left(P(u,\xi)\Big/\iint P(u,\xi)\mathrm{d}u\mathrm{d}\xi\right)^a \mathrm{d}u\mathrm{d}\xi \tag{47}$$

The Rényi entropy will decrease with the improvement of concentration. In this paper, the third-order Rényi entropy is used to quantitatively measure the TF energy concentration. The TFRs and corresponding Rényi entropies of SST and TSST at different chirp rates are shown in Fig. 5. It can be found that for signal with low chirp rate (200 Hz/s), the concentration of
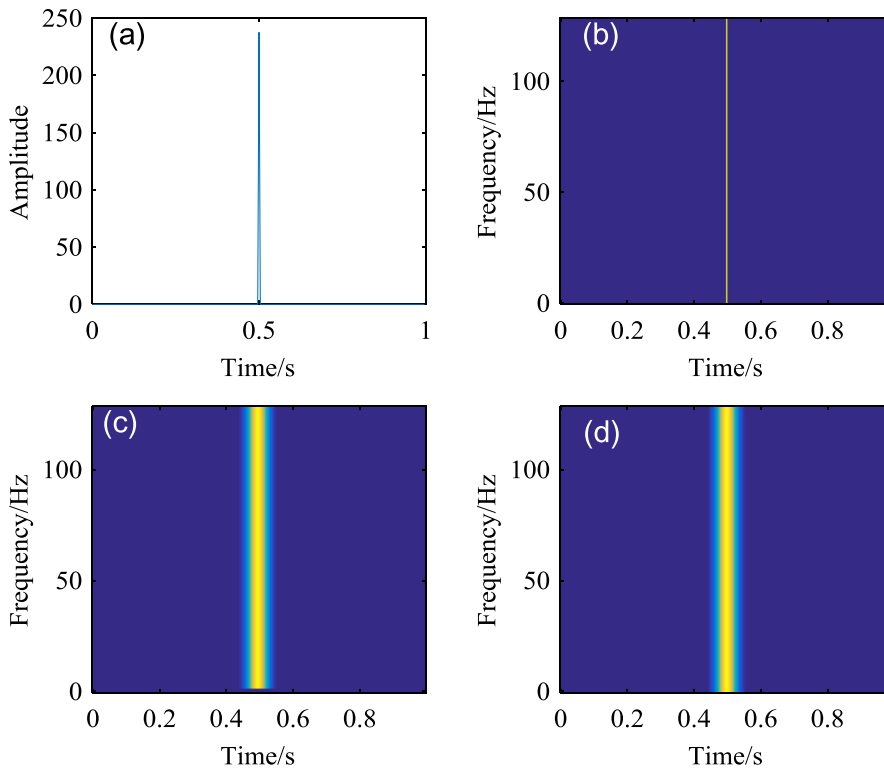

Fig. 4. The illustration of the property of the TSST towards the ideal TFR; (a) impulsive-like signal; (b) TSST; (c) SST; (d) STFT.

Table 1
Parameters of the simulated signal and analytical parameters.

	Parameters	Names	Values
Signal parameters	t_0	central time	0.5 s
	f_0	central frequency	250 Hz
	σ_0	Gaussian standard deviation	0.05 s
	c	chirp rate	200, 400, 600 Hz/s
Analytical parameters	f_s	sampling frequency	1024 Hz
	N	number of sampling point	1024
	σ	standard deviation of window function	0.02 s

SST is better than TSST; for signal with medium chirp rate (400 Hz/s), the Rényi entropy of SST is approximately equal to TSST; for signal with high chirp rate (600 Hz/s), the TSST is superior to SST. Thus, the proposed TSST can effectively improve the TF energy concentration of signal whose chirp rate is very large.

It can be inferred from Fig. 5 that there is a boundary on which the performance of TSST and SST is the same. On the one side of the boundary, TSST performs better and on the other side of the boundary, SST wins. The parameters selection strategy will be obtained if the boundary is found, which provides a specific direction for selecting either SST or TSST. In order to investigate the effect of parameters c and σ on TFR, we fix all the parameters except c and σ. The methods of TSST and SST are implemented at different c and σ.

Fig. 6 shows the Rényi entropy vs. σ map of SST, TSST and STFT at different chirp rates. It can be observed that for a signal with fixed chirp rates, SST and TSST have respective ranges of σ where the TFR is more concentrated. The SST outperforms
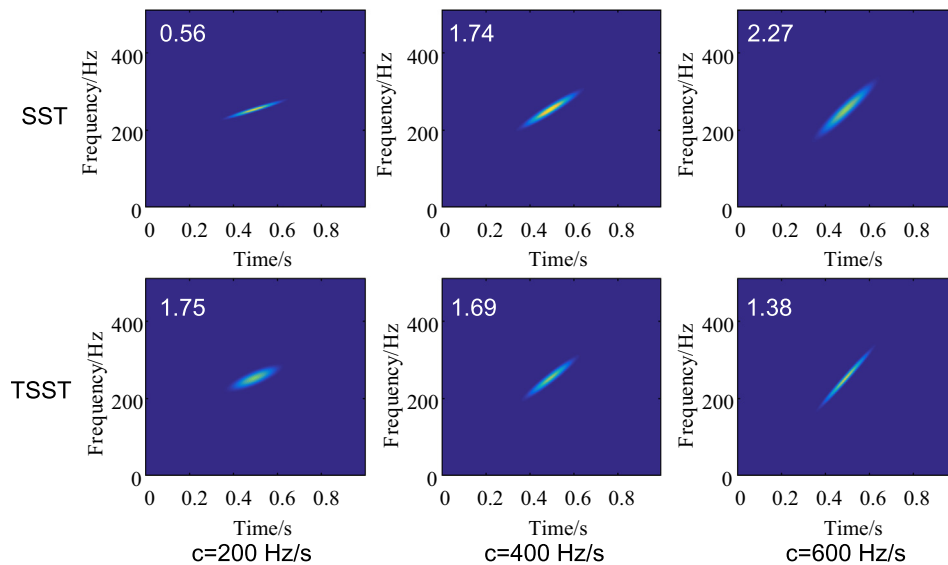
Fig. 5. SST and TSST at different chirp rates and their Rényi entropies (white numbers).
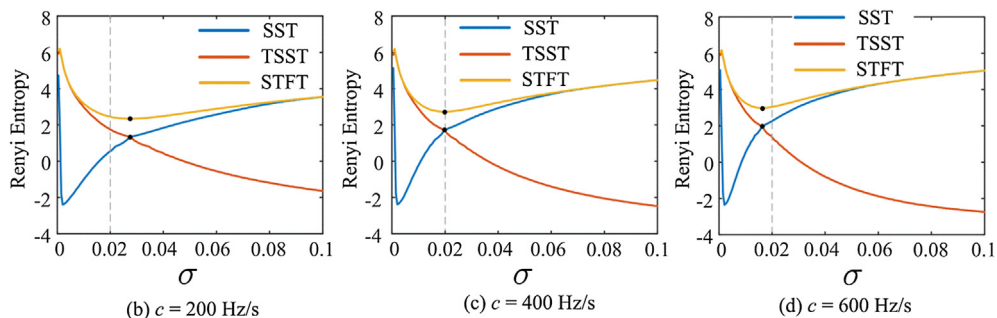
Fig. 6. Rényi entropy vs. σ of SST, TSST and STFT at (a) c = 200 Hz/s; (b) c = 400 Hz/s; (c) c = 600 Hz/s.

TSST at a narrow window while TSST is superior at a wide window (narrow window in the frequency domain). Therefore, there is an intersection where SST and TSST perform the same. However, it is somewhat difficult to determine the σ at the intersection between the SST and TSST.

As shown in Fig. 6, the valley point on the curve of STFT means an optimal standard deviation of a Gaussian window. It can be found that the optimal standard deviation of STFT visually equals the σ at the intersection of SST and TSST. In order to strengthen our finding, we can draw a three-dimensional diagram in the parameter space $\Sigma \times C$, where $\Sigma = \{\sigma | \sigma = 0:0.0005:0.05\}$, $C = \{c | c = 0:10:2000\}$, as shown in Fig. 7. The intersection curve of SST and TSST can be obtained easily. Then Fig. 8 shows the intersection curve and the valley curve of STFT overlap with each other on the c-σ plane. Therefore, our aim is to find the analytical form of the valley curve of STFT, i.e., the optimal time-frequency Gaussian window. Fortunately, Ref. [41] illustrates that the optimal time-varying standard deviation of a Gaussian window of STFT is approximately described as

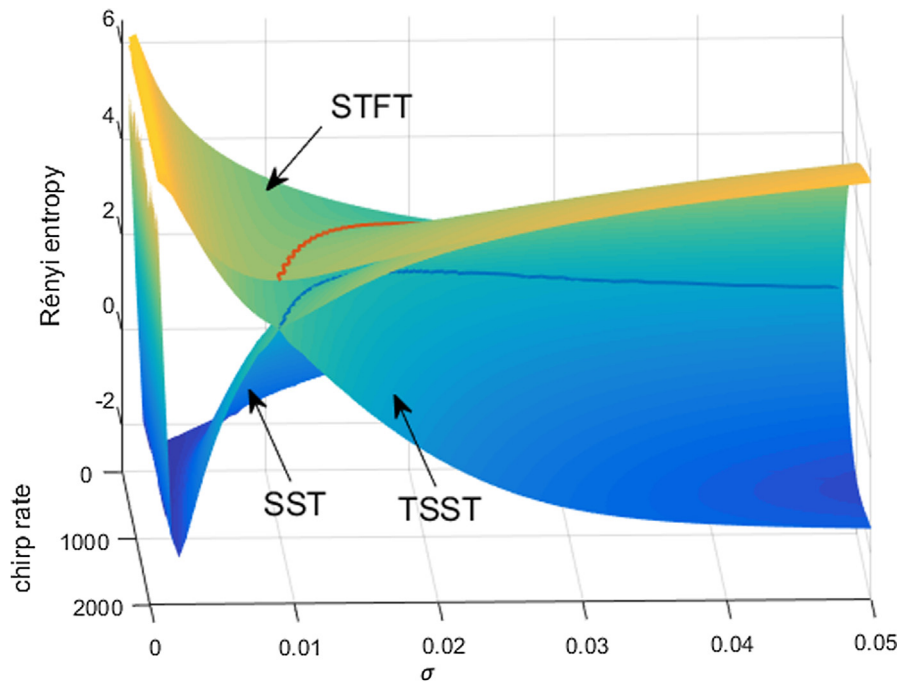$$\sigma(t) \approx \frac{1}{\sqrt{2\pi\phi''(t)}} \tag{48}$$

Fig. 7. Rényi entropy of SST, TSST and STFT in parameters space $\Sigma\{0:0.0005:0.05\} \times C\{0:10:2000\}$.
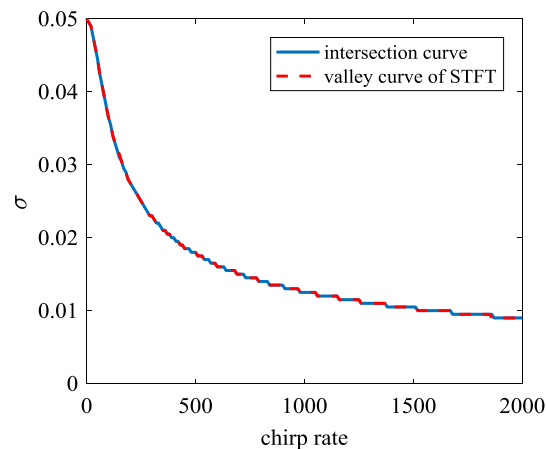

Fig. 8. The intersection curve and the valley curve of STFT projected on the c-σ plane.

where $\phi(t)$ denotes the phase of the signal and $\phi''(t)$ denotes the change rate of instantaneous frequency, i.e., the chirp rate. In this simulation, the chirp rate is c. Thus we have

$$\hat{\sigma}_t \approx \frac{1}{\sqrt{2\pi c}} \tag{49}$$

where $\hat{\sigma}_t$ is the optimal standard deviation of a Gaussian window. It can be observed from Fig. 9 that on the upper side of the curve, TSST performs better, while SST wins on the lower side of the curve. For signals whose chirp rate is small, it is likely to use SST because SST has a wider parameter selection range; for signals with large chirp rate, TSST has a wider parameter selection range.

On the other hand, impulsive-like signals is modeled more easily in frequency domain as

$$x(t) = F^{-1}\left\{ \sum_{k=1}^{K} A_k(\omega)e^{i\varphi_k(\omega)} \right\} \tag{50}$$

where $F^{-1}\{\cdot\}$ denotes the inverse Fourier transform; $A_k(\omega)$ and $\varphi_k(\omega)$ denotes the amplitude and phase vs. frequency of the kth component of the signal $x(t)$, respectively. The $\varphi_k'(\omega)$ is called GD and $\varphi_k''(\omega)$ is called group delay modulation. Therefore, on the time-frequency ridge in Fig. 10, time and frequency are restricted by a function. It can be seen that $\phi_k'(t)$ and $\varphi_k'(\omega)$ are mutually inverse functions, so we have

$$|\varphi''_k(\omega)| = \left| \frac{1}{\phi''_k(t)} \right| \tag{51}$$

For signals whose chirp is very large, i.e.

$$|\phi''_k(t)| > \frac{1}{\varepsilon_1} \tag{52}$$

SST will get blurred, but TSST can obtain satisfied TFR because

$$|\varphi''_k(\omega)| = \left| \frac{1}{\phi''_k(t)} \right| < \varepsilon_1 \tag{53}$$
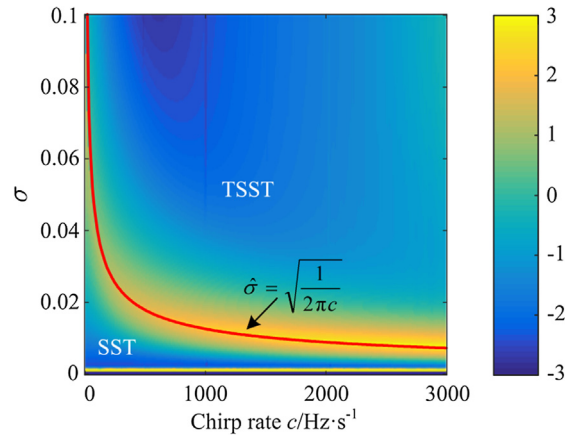

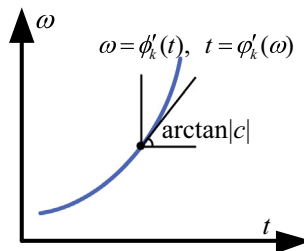**Fig. 9.** Parameters selection for SST and TSST.

Fig. 10. Time-frequency ridge.

which means strong time-varying signal in time-domain becomes weak *frequency-varying* in the frequency domain. Therefore, the TSST can be employed to represent the signals whose chirp is very large. However, this is not to say that TSST is superior to SST. For example, the standard SST can get reasonable results when $|\phi''_k(t)| < \varepsilon_1$. If TSST is employed in this case, the concentration of TFR will decrease, which means that the change-rate of GD $|\varphi''_k(\omega)|$ is so large that TSST cannot characterize the TFR correctly. Thus, the TSST and SST have respective application scope and they are complementary methods.

5. Applications

In this section, several simulation and application cases are presented to demonstrate the performance of TSST for GD extraction and mode reconstruction. The effectiveness of the TSST for fault diagnosis is also verified by experimental study.

5.1. Simulation study on lamb wave

Lamb wave can be regarded as impulsive-like signal mentioned above, which is multimodal and highly dispersive. Obviously, TFA methods are promising tools for determining the dispersion curves of lamb wave to extract information of the structure because the dispersion curves of broadband multiple modes can be obtained from just single measurement [42]. The use of TFA methods can directly characterize multiple group velocities (a function of frequency) of propagation mode hidden in lamb wave which overlaps in the time-domain. Tradition linear or quadric TFA methods such as STFT [43], CWT [43] and Pseudo WVD [42,44] were adopted to analyze Lamb waves. The RSTFT was also introduced for improvements of dispersion curves of lamb wave, enhancing the readability of TFR [45–48] but it failed to retrieve individual modes. Niethammer et al. compared the RSTFT, RWT, (smoothed) WVD and EMD of lamb waves and drew a conclusion that the RSTFT performed best among these methods [45]. Further, Yang et al. employed generalized warblet transform to characterize strongly nonlinear dispersion trajectories of different modes with high concentration TFR, but the prior knowledge of the theoretical dispersion trajectories was needed [49]. In addition to the TFR of lamb waves, mode separation of lamb waves is also important after the ridges curves are obtained since it allows for the development of new measurement applications [50]. Xu et al. [51] proposed a method of dispersion compensation for mode separation. The method compresses each dispersive mode into temporal pulses and extracts each mode by rectangular time windows, but the wave-number was required in advance. Further, they proposed a crazy-climber algorithm to extract time-frequency ridges along the time axis of individual modes for adjacent reconstruction [52]. On the other hand, one can use ridge extraction method along frequency axis rather than time axis for better mode separation results. In this case, the TSST can obtain relatively high concentrated TFR, and more importantly, without the prior knowledge required. In this subsection, the proposed TSST and its inverse transform are applied in the simulation of the Lamb waves and the performance of the TSST is also compared with other TFA methods.

The dispersion curves of lamb wave of mode S0 and A0 are shown in Fig. 11(a), in which the group velocity curves are presented. The group delay $t_{g,k}$ of the kth component respect to frequency can be calculated by group velocity curve $c_{g,k}$

$$t_{g,k}(f) = \frac{L}{c_{g,k}(f)} \tag{54}$$

where L denotes the distance of propagation with $L = 0.1$ m. The thickness of plate d is 1.5 mm. Fig. 11(b) shows the ideal time-frequency relation of each mode of lamb wave in the TF plane. It can be found that the curves are almost vertical in time-frequency plane, thus the signal can be used to test the performance of the proposed TSST compared with other TFA methods. Then, the spectrum of lamb wave with K modes can be constructed in the frequency domain as

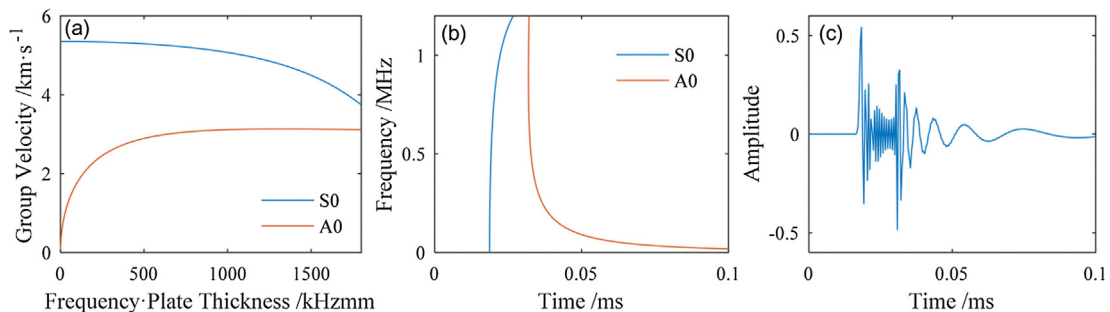$$\hat{x}(f) = \sum_{k=1}^{K} \exp\left(i2\pi \int t_{g,k}(f)\mathrm{d}f\right) \tag{55}$$

Fig. 11. Simulation study on lamb wave. (a) the dispersion curves of lamb wave; (b) the TF structure of Lamb wave; (c) Lamb wave in time domain.

For convenient, transforming the signal into time domain is implemented using inverse DFT

$$x(t) = F^{-1}(\hat{x}(f)) \tag{56}$$

Fig. 11(c) shows the lamb wave with modes S0 and A0 in the time domain, and it is an impulsive-like signal obviously. In this simulation case, the Gaussian function

$$g(t) = (\pi\sigma^2)^{-1/4} e^{-t^2/\sigma^2} \tag{57}$$

with $\sigma = 3.5 \times 10^{-6}$ is used as the window function. The proposed TSST is compared with different TFR methods such as STFT, SST, and RSTFT (one kind of STFRM but non-invertible TFA method). The Fig. 12(a) illustrates the STFT result. It can be seen that the TFR obtained by the STFT has a low TF energy concentration, in which the two modes cannot be separated clearly. The SST is used to improve the TF energy concentration. However, the TF concentration of SST in Fig. 12(b) cannot show any improvement, especially the "vertical part" of the curves. At the "horizontal part" of the mode of A0, SST gives a relatively satisfactory performance. On the contrary, the TSST result shown in Fig. 12(d) illustrates that the TF concentration is improved, especially for "vertical part" of the curves. However, TSST's performance decreases at the "horizontal part" of the mode of A0. It can be seen that the SST is suitable for characterizing the "horizontal part" of the curves in TF plane while TSST is suitable for characterizing the "vertical part". Even though the, energy concentration of the RSTFT result is greatly improved in Fig. 12(c), the RSTFT cannot be reconstructed and it is time-consuming. The elapsed time of TSST, SST and RSTFT after 20 averages is listed in Table 2.

The robustness of TSST is studied by adding white Gaussian noise to the simulated signal. The noisy signal with SNR = 0 dB is analyzed by TSST and the other TFA methods. The same parameters used for the noise-free signal are used here to obtain the STFT, SST, RSTFT, and TSST representations, as shown in Fig. 13. The visual interpretation shows that the TSST is robust to noise without losing obvious concentration.

The most important property of TSST over RSTFT is invertibility. Fig. 14 shows each mode and their reconstruction waveforms of the simulation signal with SNR = 0 dB. Before reconstruction, the TSST (Fig. 14(a) and (d)) is time-frequency filtered
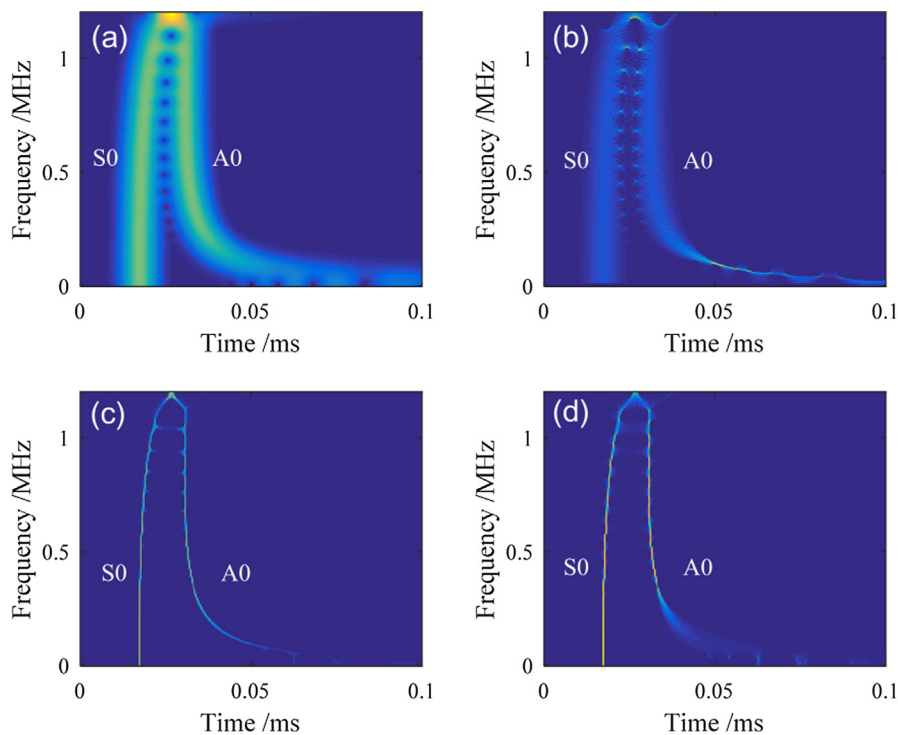

Fig. 12. The TFRs of the noise-free signal obtained by (a) STFT, (b) SST, (c) RSTFT, (d) TSST.

Table 2
Elapsed time of TSST, SST and RSTFT.

	TSST	SST	RSTFT
Elapsed time (s)	0.1546	0.1919	0.3208

to extract the mode to be separated. We select a time-frequency zone in which the "center line" is the kth GD and the fixed time width is $2d$. The TSST representation is very concentrated, so that the choice of the width of the zone is not crucial, which means the results remain the same for a wide range of choices for this width [11]. The time-frequency coefficients in this zone keep their value while the other time-frequency coefficients outside it are set to 0. Thus, the time-frequency zone which we are concerned about is selected and retained, as shown in Fig. 14(b) and (e). Then integrate $V_x[m, k]$ over the corresponding subregion of the time domain to obtain the spectrum of the signal. Fig. 14 shows the zones selected in the TSST plane as well as the corresponding reconstructed components. It can be seen that for this type of impulsive-like signal, the proposed TSST seems to give an interpretable result.

In order to further demonstrate the robustness of the TSST, a series of noises with different SNR levels from 20 dB to −5 dB are added into the simulation signal. Fig. 15 shows the Rényi entropies of the TFRs. It can be found that the Rényi entropies always increase with the noise, which means the noise degrades the energy concentration of these TFRs. As shown in Fig. 15, the Rényi entropy of the TSST is less than the Rényi entropies of the SST and STFT. Even though the RSTFT gives lowest Rényi entropy in Fig. 15, it is irreversible and time-consuming. Consequently, the TSST can improve the TF concentration and keep invertible simultaneously.

The robustness of the TSST reconstruction is validated by adding a series of noises with different SNR levels from 20 dB to −5 dB into the simulation signal. The reconstruction performance is evaluated by the reconstruction SNR which is defined as:

$$SNR = 10 \log \left\{ \| x(t) \|^2 / \| x(t) - \hat{x}(t) \|^2 \right\} \tag{58}$$

where $x(t)$ and $\hat{x}(t)$ denote the noise-free signal and reconstructed signal, respectively. Fig. 16 shows the corresponding SNR of the reconstructed signal with respect to the input SNR. In this case, the TSST is compared with SST and STFT. It can be found that the reconstruction SNR decreases with the noise, which means the noise degrades the reconstruction performance of all these methods. Moreover, it can be also found that the reconstruction SNR of the TSST is larger than the other TFRs, especially when the input SNR is less than -2 dB. Therefore, it can be concluded that, compared with SST and STFT, the TSST can improve the reconstruction accuracy of the signal for denoising or separating modes.

5.2. Experimental study on rub-impact fault diagnosis

Impulsive-like signals exist extensively in mechanical fault diagnosis fields such as localized rub-impact, where the transient feature is what we concerned. Localized rub-impact is a common and serious fault in rotor systems and it can be modeled by coupled modeling of rolling bearing-rotor systems [53]. The rub-impact phenomenon occurs when a rotating part
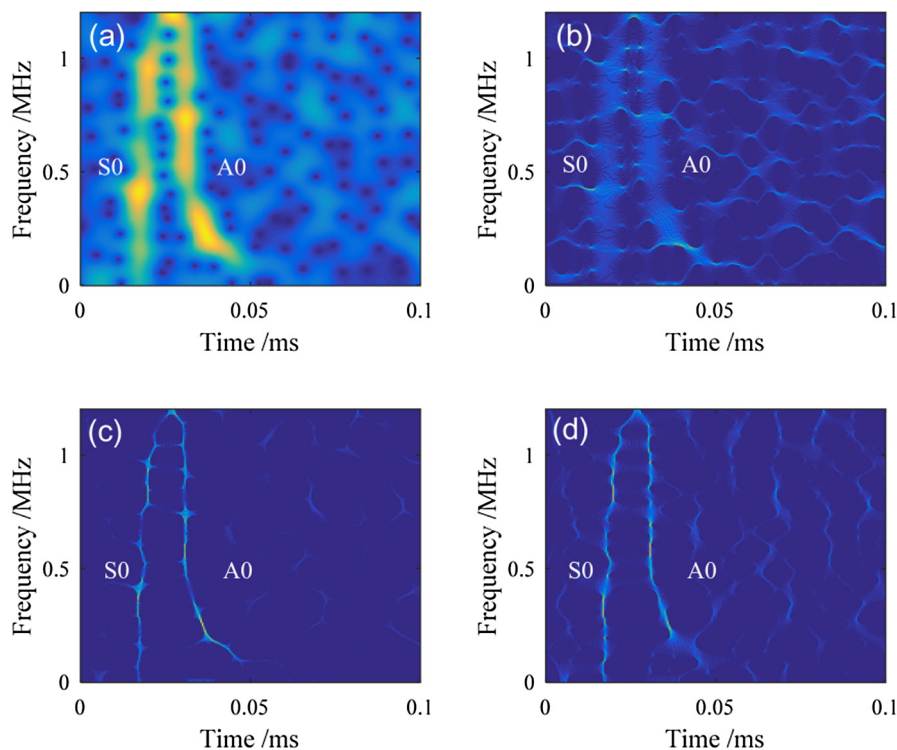

Fig. 13. The TFRs of the noisy signal with SNR = 0 dB obtained by (a) STFT, (b) SST, (c) RSTFT, (d) TSST.
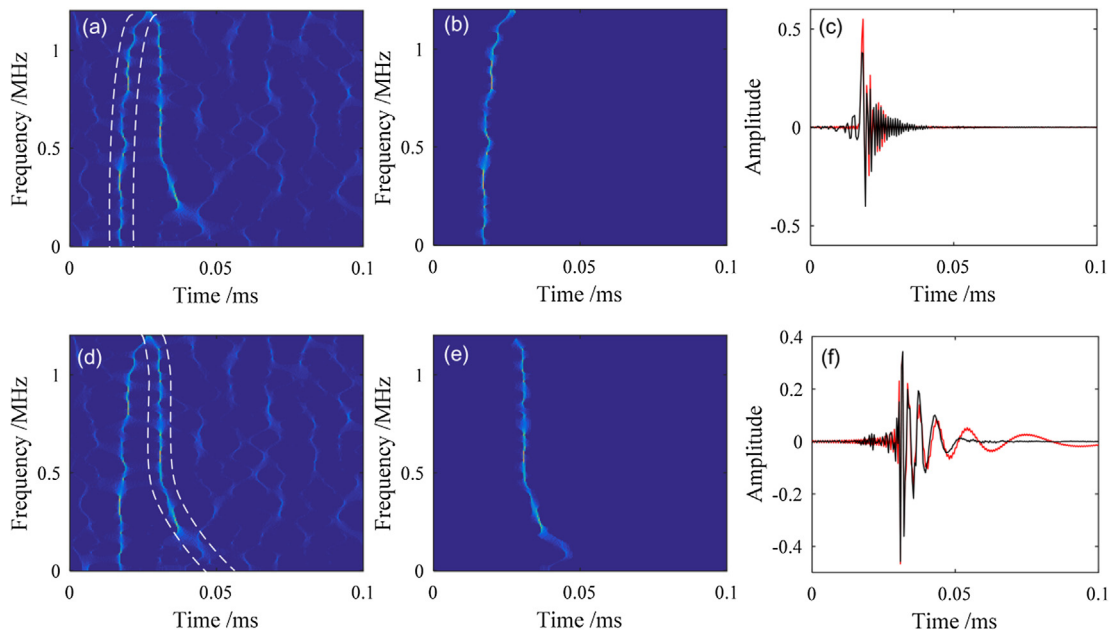
Fig. 14. Reconstruction signal of mode S0 and A0 with SNR = 0 dB. (a), (d) zone marked on the TSST for reconstruction of the modes; (b) mode S0 filtered out from TSST; (c) S0 reconstruction waveform (in black), noise-free original waveform (in red); (e) mode A0 filtered out from TSST; (f) A0 reconstruction waveform (in black), noise-free original waveform (in red). (For interpretation of the references to colour in this figure legend, the reader is referred to the web version of this article.)
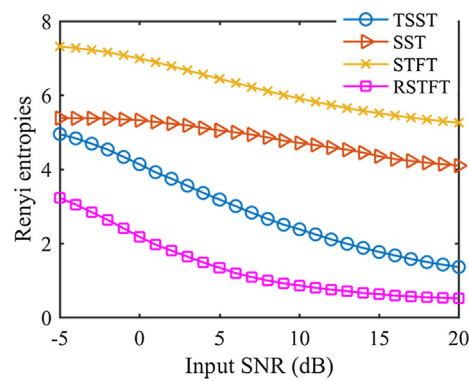

Fig. 15. Rényi entropies of the TFRs of the simulation signal with different noise level from 20 dB to −5 dB.
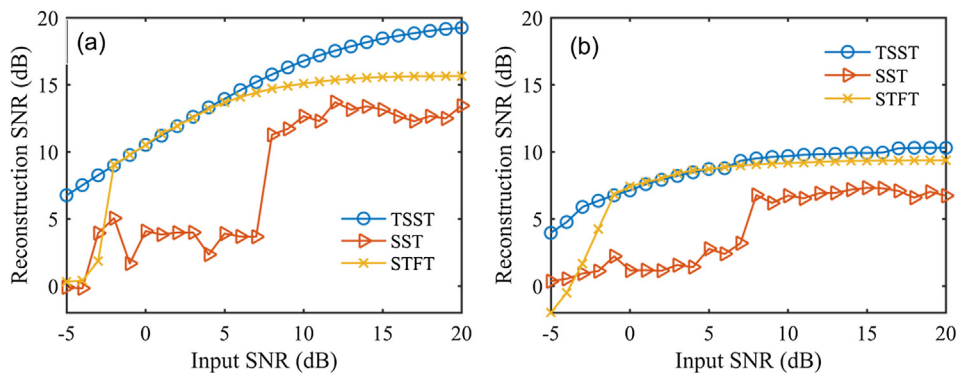

Fig. 16. The signal reconstruction by different TFR methods for the mode (a) S0 and (b) A0 with different noise level from 20 dB to −5 dB.

hits the stationary part periodically. On the other hand, the rub-impact feature can also be extracted via some advanced signal processing methods. The impulsive feature for each hit appears in localized rub-impact conditions and their signals can be regarded as impulsive-like signals. Therefore, it is necessary to employ TFA methods to determine the exact occurrence time of each impulsive signal to indicate the transient feature caused by rub-impact. The transient feature of rub-impact was extracted by reassigned scalogram i.e. RWT [54,55]. The energy of impacts was collected along both scale and time direction. The result showed that a vertical line appears as the rotor hit the stationary part and the severity of the rub-impact can be reflected by the width of the frequency band. However, the reassign operation was conducted in two directions, which requires more computation cost. For rub-impact fault diagnosis, what we usually concern is the occurrence time of each impulsive signal and sometimes we need an invertible process to extract fault features in the time domain.

In this subsection, the proposed TSST method is firstly applied in rub-impact fault diagnosis on a Bently test rig, as shown in Fig. 17. The test rig consists of a motor, a rotor with initial unbalance, two displacement sensors (Bentley 3300 XL 8 mm with sensitivity 7.87 V/mm). The Tektronix signal generator produced voltage, which was input to the Bently speed controller's external input port to control the speed of the DC motor. The input voltage of the Bently speed controller varied from 0 to 5 V, corresponding to the rotational speed from 0 to 10,000 R/MIN. The rub-impact fault was introduced by a brass screw, which was placed close to the shaft to produce localized rub-impact faults. The rotor vibration signal was collected by two displacement sensors perpendicular to each other and a data acquisition system. The sampling frequency was 2560 Hz and the rotational speed of the rotor was 1200 r/min and 1500 r/min.

Fig. 18(a) shows the time waveform of the vibration signal with localized rub-impact fault at 1200 r/min. It can be observed that the slight distortion of its shape, but it is hard to determine the exact occurrence time of each impact. The spectrum shown in Fig. 18(b) has the second harmonic of rotational frequency as the distortion of the signal.

The proposed TSST method is applied to extract the transient feature resulted by each hit. In this case, the Gaussian function in with $\sigma = 0.005$ is used as the window, and the TSST result is shown in Fig. 18(c). It can be observed from the TSST representation that the TF energy is more concentrated, from which we can see the occurrence time of each impact clearly. The time interval of successive impact is the rotational period, which means the rotor hits the screw once per revolution. Consequently, this periodic transient feature provides evidence to judge the existence of the localized rub-impact fault in the rotor system.

For the purpose of comparison, STFT, SST, and RWT are also used to analyze the vibration signal. The window function in STFT and SST is the same as that in TSST, and time-bandwidth product of the mother wavelet in RWT is 1. The TF representations obtained by STFT, SST, and RWT methods are shown in Fig. 18(d)–(f), respectively. The vertical lines of STFT are blurred and it is hard to determine the time intervals between them. The SST relocates the TF energy along frequency axis with which the curves of the impulsive-like signal are parallel. Thus the TFR accuracy is decreased using SST and the TF energy becomes disordered for interpretation. As one kind of STFRM, RWT reassigned the TF energy along time axis to sharpen the vertical curve in Fig. 18(d). However, it weakens the transient features of the pulse due to additional reassignment along the frequency axis. Moreover, the RWT cost more time than TSST, as shown in Fig. 20. After 50 averages, the time cost of SST and TSST is less than 10 s because of one-dimensional integral while the time cost of RWT is nearly 30 s due to its two-dimensional integral. Through the comparison results, it can be concluded that the TSST can extract the transient feature produced by rub-impact more effectively than the STFT, SST, and RWT.

The same rule still holds when the rotational speed is 1500 r/min, as shown in Fig. 19. The slight difference from Fig. 18 is that the seriousness of rub-impact increases with speed. This is because the contact force between the unbalanced rotor and stationary part increases with the amplitude of vibration, which is affected by the rotational speed. In the spectrum of the vibration signal, the percentage of the second harmonic is higher than that in 1200 r/min, which indicates the seriousness of rub-impact. Especially in Fig. 19(c), the rub-impact fault at 1500 r/min excites more high-frequency components so the
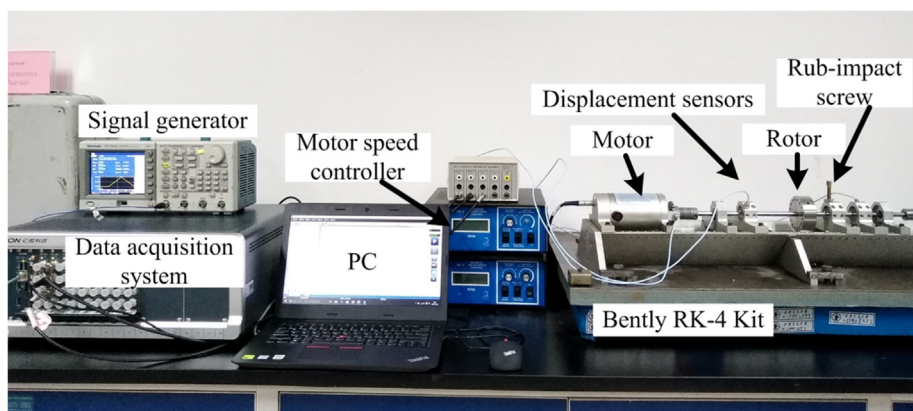

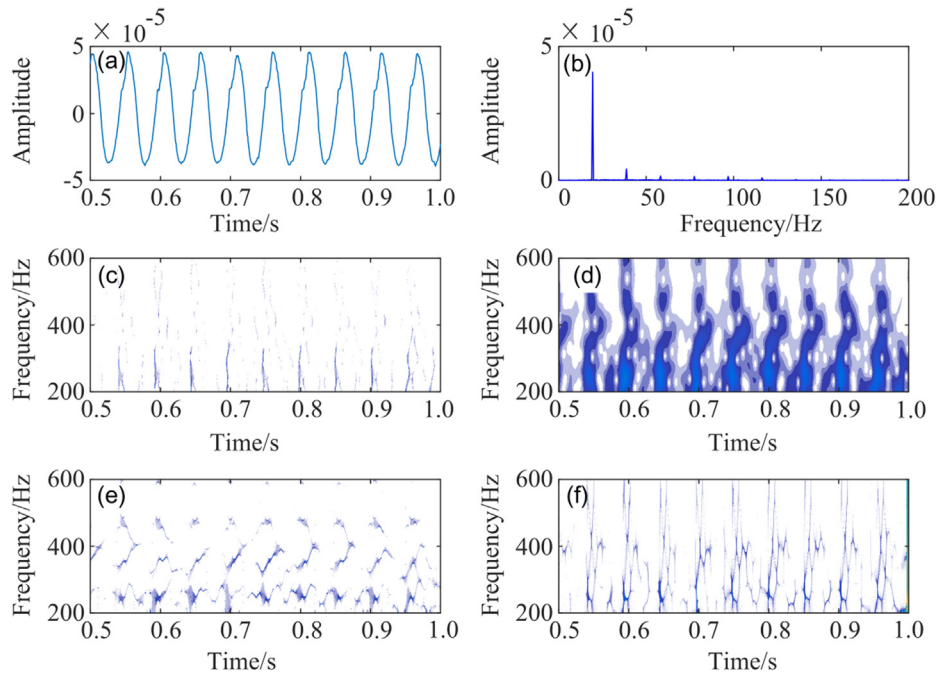**Fig. 17.** Experimental setup of the Bentley rotor test rig.

Fig. 18. Localized rub-impact fault at 1200 r/min. (a) time waveform; (b) spectrum; (c) TSST; (d) STFT; (e) SST; (f) RWT.
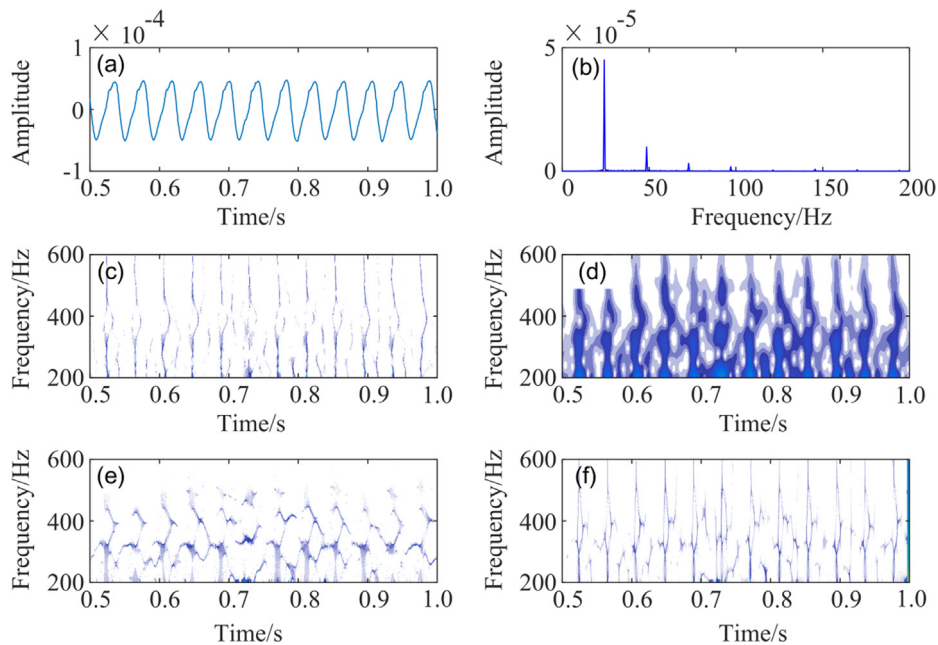

Fig. 19. Localized rub-impact fault at 1500 r/min. (a) time waveform; (b) spectrum; (c) TSST; (d) STFT; (e) SST; (f) RWT.

vertical curve stretch to higher frequency band than that in Fig. 18(c). Additionally, the time interval between adjacent pulses is narrower than that in 1200 r/min due to higher rotational speed.

5.3. Application in air compressor fault diagnosis

In this section, the TSST is applied in air separator and compressor fault diagnosis for transient feature extraction [56]. The structure of the air separation and compression set is shown in Fig. 21. In the gearbox, the pinion was designed to own an anti-thrust plate at each end to bear the axial force. The vibrational level of the gearbox exceeded the limit after an overhaul.
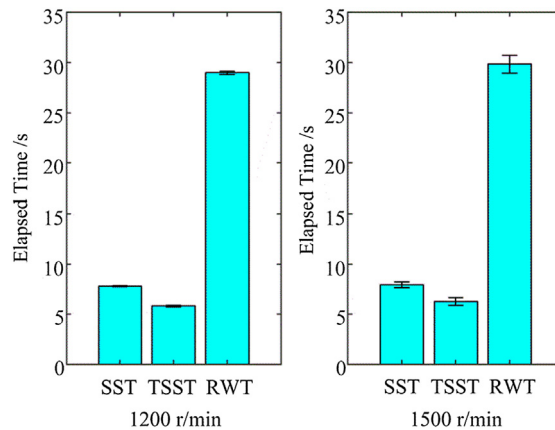
Fig. 20. Elapsed time after 50 averages.

In order to explore the root of the vibration and noise, the vibration acceleration signals were collected from a bearing pedestal of the gearbox. The rotational speed of the motor on Shaft I was about 2985 r/min (49.75 Hz) and the rotational frequency of shaft II was 213 Hz. This means the working frequency of the compressor is 213 Hz. The meshing frequency of the gearbox was 6815.75 Hz. The sampling frequency was 15 kHz and the number of sampling point is 1024. The time domain acceleration signal is shown in Fig. 22(a), in which the peak-peak value is nearly 1000 m/s^2 and the transient pulse due to rub-impact seems to be masked by noise. Fig. 22(b) shows the spectrum of the vibration signal, in which the frequency interval of many dominant components is 213 Hz. Thus, it can be inferred that the vibration is caused by shaft II.

The vibration signal was further analyzed by TSST with $\sigma = 2.5 \times 10^{-4}$, as shown in Fig. 22(c). It can be observed in Fig. 22 (c) that some dominant vertical curves occur periodically, which are aligned with the indistinct pulse in Fig. 22(a). Moreover, the time interval of these vertical curves is about 0.0047 s, which is the period of shaft II. This periodic transient feature extracted from TSST is relevant to the impact caused by some elements of shaft II. The TF energy around 2500–4000 Hz is more apparent since the impact excited the natural frequency of some elements.

After disassembling the gearbox, the pinion was found angular misaligned with the shaft II. Therefore, the end face of the anti-thrust plate was not parallel with that of the driving gear on shaft I. For every revolution of the shaft II, the installed left anti-thrust plate rubbed the left end face of the driving gear once, which caused serious vibration. However, the right anti-thrust plate did not rub the driving gear as the clearance between the right anti-thrust plate and the driving gear is wider. In this condition, the frequency of the rub-impact is equal to the rotational frequency of shaft II. Fig. 24 illustrates the rub-impact phenomenon between the anti-thrust plate on the pinion and the driving gear.

For the purpose of comparison, STFT, SST and RWT are also used to analyze the vibration signal of rub-impact. The window function in STFT and SST is the same as that in TSST, and time-bandwidth product of the mother wavelet in RWT is 2.5. The TF representations obtained by STFT, SST, and RWT methods are shown in Fig. 22(d)–(f), respectively. The STFT gives blurred TFR and the time instants are undetermined. For SST and SWT, the reassignment operation along frequency axis destroys the transient features of each pulse caused by the fault and makes it disordered for interpretation.

For the comparison of computational efficiency, the computational time of TSST, SST, and RWT are shown in Fig. 23. After 100 averages, the time cost of SST and TSST is far less than that of RWT. Through the comparison results, it can be concluded that the TSST representation behaves better than the STFT, SST, and RWT.

From this application, we can find that the proposed TSST could provide satisfied energy concentrated TFR with excellent transient features for rub-impact fault diagnosis.
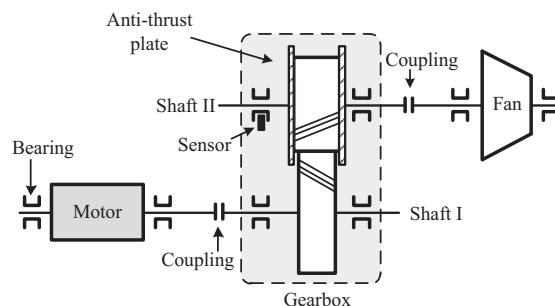

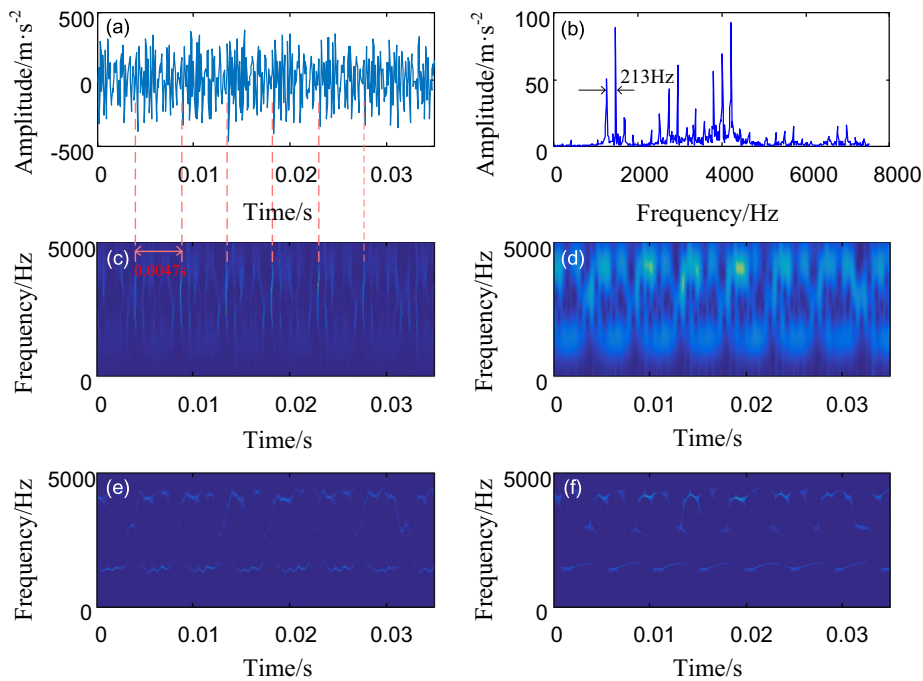**Fig. 21.** The schematic sketch of the oxygen separation and compression unit.

Fig. 22. Application to air compressor fault diagnosis. (a) time domain acceleration signal and its (b) spectrum; (c) TSST; (d) STFT; (e) SST; (f) RWT. The vertical curves in (c) are aligned with indistinct pulses in (a).
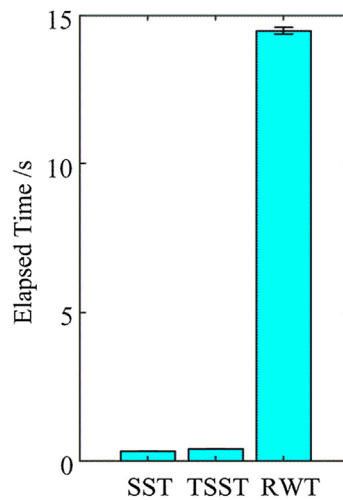

Fig. 23. Elapsed time after 100 averages.

6. Discussion

From the simulation and fault diagnosis applications, it can be concluded that the TSST is effective in characterizing impulsive-like signals. We now discuss the parameter selection, order extension, and reconstruction property.

6.1. Selection of σ_t

In Section 3.2, TSST is compared with the original SST and the parameter selection range for σ_t is given. It should be pointed that the range in Fig. 9 is only for mono-component signal, as it is unnecessary to consider mode aliasing.
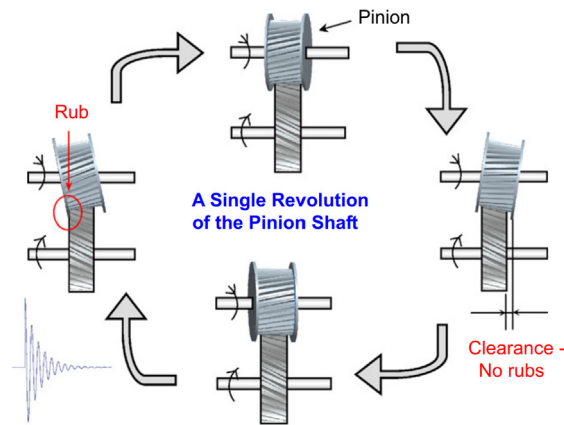
Fig. 24. Illustration of rub-impact between the left anti-thrust plate of the pinion and the driving gear [56].

Thus, the time-frequency concentration is the only objective function to maximize. However, for multi-component signals, separation property of TFR must be also considered. The balance should be obtained between the separation property and concentration. Generally speaking, for multi-component harmonic-like signal, one should select relatively small σ_t for better concentration of SST but relatively large σ_t for separation property. The aliasing phenomenon is likely to occur at frequency axis, so the σ_t has a lower bound for selection. However, for multi-component impulsive-like signal, too large σ_t will cause mode aliasing at time axis. In this condition, the σ_t has an upper bound for selection. Therefore, there is a bound to restrict the selection of σ_t, i.e., the σ_t cannot be selected in the shadow area as shown in Fig. 25.

6.2. Extension of TSST towards second order

In this paper, the GD estimator is calculated by STFT and its partial derivative respect to frequency. However, the IF estimator is neglected since the TSST only uses GD estimator to reassign the TF energy along the time axis. If the ideal TF curve is distorted far from the impulsive-like feature, like the end section of A0 mode in Fig. 11(c), the concentration of TSST will decrease sharply. Although RSTFT method can relocate energy for a sharper TFR both considering GD and IF estimator, the reconstruction of RSTFT is absent. Thus, it is necessary to refine the proposed TSST to retain good concentration and invertibility for a more general kind of signal. From the point of the SST framework, the approximation order is one for original SST, in which only the IF estimator was calculated. However, in MSST proposed in Ref. [21], apart from IF estimator and GD estimator, the chirp-rate estimator is also calculated. The MSST is superior to original SST in concentration and invertibility as the approximation order is two for MSST, which is higher than SST. Similarly, for a better TFR, TSST can also be extended towards second order in the future studies.
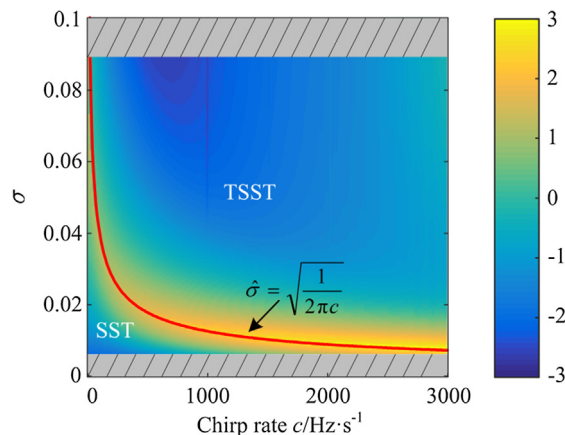

Fig. 25. The bound of selection of σ_t for a multi-component signal.

6.3. Reconstruction property

The property of signal reconstruction is the main advantage of TSST over RSTFT. In this paper, the signal reconstruction property is investigated and verified by the simulation study for mode separation of lamb wave. The property of signal reconstruction of TSST acts as a filter method here. For the application case, TFR of vibration signal with rub-impact fault could be also time-frequency filtered if needed, which followed by the inverse transform of TSST for signal reconstruction. Moreover, for some other kinds of fault features which are indicated more easily in the time domain, it is meaningful to make full use of the invertibility of TSST for denoising or decoupling from unwanted components. This cannot be implemented using RSTFT. Thus, the reconstruction results show that the signal reconstruction of TSST is useful for fault feature extraction.

7. Conclusions

In this paper, the TSST has been presented as a powerful TFA tool for impulsive-like signals. In the TSST method, a strong time-varying signal in time-domain becomes weak *frequency-varying* in the frequency domain. For impulsive-like signals, a high-order approximation for IF in SST framework can be replaced by low-order approximation for GD in TSST framework. Therefore, the TSST provides a highly concentrated TFR for the signal whose TF ridge curves is nearly parallel with frequency axis and meanwhile allows for reconstruction as the original SST. In the algorithm of TSST, the GD estimator is calculated rather than the IF estimator. At the same time, the TSST reassigns the TFR only in the time direction, thus it retains the invertibility, which enables the signal reconstruction from the TSST representation to the frequency domain. Moreover, the efficient numerical algorithm has been described in this paper for practical implementation in the discrete form of TSST.

From the comparison between SST and TSST, we found that the SST is suitable for characterizing signal with small chirp-rate while TSST performs better for characterizing signal with large chirp-rate. Thus, TSST is more capable for a strong time-varying signal for extracting transient features but it is useless for a slowly time-varying signal. It is noteworthy that the SST and TSST are complementary with each other and each of them has respective working condition. They are all special case of RSTFT but allow mode reconstruction.

In this paper, the effectiveness of TSST and its inverse transform is validated using both simulated lamb wave and practical vibration signals. Using the TSST method, we have identified the dispersive modes of lamb wave by time-frequency ridges. The TSST gives a more concentrated TFR for impulsive-like signal, compared with other TFA methods. In addition, each mode of the simulated lamb wave is retrieved and separated accurately by time-frequency filtering and inverse TSST. In this paper, the TSST method has also been validated using both experimental and industrial vibration signals for rub-impact fault diagnosis. Using the TSST method, we have identified the periodical transient feature caused by localized rub-impact fault on Bently test rig, in which the impulsive period is the reciprocal of the rotational frequency of the rotor. The practical implementation of TSST on the vibrational signal of an oxygen separator and compressor set has successfully diagnosed the rub-impact fault caused by misalignment between the pinion the shaft. To sum up, simulation and experimental results have demonstrated the effectiveness of TSST for characterizing transient feature in mechanical signal processing.

Appendix A

In this appendix, we will demonstrate that $\hat{\omega}_x(u,\xi)$ and $\hat{t}_x(u,\xi)$ can be interpreted as the center of gravity of signal's energy distribution around TF point (u,ξ). On the other hand, $\hat{\omega}_x(u,\xi)$ and $\hat{t}_x(u,\xi)$ can be also defined by the partial derivatives of the phase of STFT.

Firstly, the STFT can be defined as

$$S_x^g(u,\xi) = \int x(t)g(t-u)e^{-i\xi(t-u)}\mathrm{d}t = M_x^g(u,\xi)e^{i\Phi_x^g(u,\xi)} \tag{59}$$

where $M_x^g(u,\xi)$ and $\Phi_x^g(u,\xi)$ denotes the magnitude and phase of $S_x^g(u,\xi)$.

Then, the center of gravity of frequency $\hat{\omega}_x(u,\xi)$ is obtained by weighted integral

$$\hat{\omega}_x(u,\xi) = \frac{\iint \omega \cdot Q_{u,\xi}(t,\omega)\mathrm{d}t\mathrm{d}\omega}{\iint Q_{u,\xi}(t,\omega)\mathrm{d}t\mathrm{d}\omega} \tag{60}$$

where the weight is $Q_{u,\xi}(t,\omega) = \frac{1}{2\pi}x(t)g(t-u)\hat{x}(\omega)\bar{\hat{g}}(\omega-\xi)e^{-i\xi(t-u)}e^{-i\omega u}$ and it can be regarded as the probability distribution function around TF point (u,ξ). Then we obtain

$$\frac{\iint \omega \cdot Q_{u,\xi}(t,\omega)dtd\omega}{\iint Q_{u,\xi}(t,\omega)dtd\omega} = \frac{\iint x(t)g(t-u)\omega\hat{x}(\omega)\hat{g}(\omega-\xi)e^{-i\xi(t-u)}e^{-i\omega u}dtd\omega}{2\pi S_x^g(u,\xi)\cdot S_x^g(u,\xi)}$$

$$= \frac{\int x(t)g(t-u)e^{-i\xi(t-u)}dt\cdot\int \omega\hat{x}(\omega)\hat{g}(\omega-\xi)e^{i\omega u}d\omega}{2\pi S_x^g(u,\xi)\cdot S_x^g(u,\xi)}$$

$$= \frac{S_x^g(u,\xi)\cdot\int \omega\hat{x}(\omega)\hat{g}(\omega-\xi)e^{i\omega u}d\omega}{2\pi S_x^g(u,\xi)\cdot S_x^g(u,\xi)}$$

$$= \frac{\int i\omega\hat{x}(\omega)\hat{g}(\omega-\xi)e^{i\omega u}d\omega}{-i2\pi S_x^g(u,\xi)}$$

$$= \frac{\partial_u\int \hat{x}(\omega)\hat{g}(\omega-\xi)e^{i\omega u}d\omega}{-i2\pi S_x^g(u,\xi)}$$

$$= \frac{i\partial_u S_x^g(u,\xi)}{S_x^g(u,\xi)} \tag{61}$$

combined with Eq. (59), we have

$$\hat{\omega}_x(u,\xi) = \frac{i\partial_u S_x^g(u,\xi)}{S_x^g(u,\xi)} = \frac{i\partial_u M_x^g(u,\xi)e^{-i\Phi_x^g(u,\xi)}}{M_x^g(u,\xi)e^{-i\Phi_x^g(u,\xi)}}$$
$$= \partial_u\Phi_x^g(u,\xi) + i\frac{\partial_u M_x^g(u,\xi)}{M_x^g(u,\xi)} \tag{62}$$

In a similar way, the time reassignment operator $\hat{t}_x(u,\xi)$ can be obtained as

$$\hat{t}_x(u,\xi) = \frac{\iint t\cdot Q_{u,\xi}(t,\omega)dtd\omega}{\iint Q_{u,\xi}(t,\omega)dtd\omega} \tag{63}$$

Then we obtain

$$\frac{\iint t\cdot Q_{u,\xi}(t,\omega)dtd\omega}{\iint Q_{u,\xi}(t,\omega)dtd\omega} = \frac{\iint tx(t)g(t-u)e^{-i\xi(t-u)}\cdot\hat{x}(\omega)\hat{g}(\omega-\xi)e^{-i\omega u}dtd\omega}{2\pi S_x^g(u,\xi)\cdot S_x^g(u,\xi)}$$

$$= \frac{\int tx(t)g(t-u)e^{-i\xi(t-u)}dt\cdot\int \hat{x}(\omega)\hat{g}(\omega-\xi)e^{-i\omega u}d\omega}{2\pi S_x^g(u,\xi)\cdot S_x^g(u,\xi)}$$

$$= \frac{\int (t-u)x(t)g(t-u)e^{-i\xi(t-u)}dt}{S_x^g(u,\xi)} + \frac{\int ux(t)g(t-u)e^{-i\xi(t-u)}dt}{S_x^g(u,\xi)}$$

$$= \frac{i\int(-i)(t-u)x(t)g(t-u)e^{-i\xi(t-u)}dt}{S_x^g(u,\xi)} + u$$

$$= \frac{i\partial_\xi\int x(t)g(t-u)e^{-i\xi(t-u)}dt}{S_x^g(u,\xi)} + u$$

$$= u + \frac{i\partial_\xi S_x^g(u,\xi)}{S_x^g(u,\xi)} \tag{64}$$

combined with Eq. (59), we have

$$\hat{t}_x(u,\xi) = u + \frac{i\partial_\xi S_x^g(u,\xi)}{S_x^g(u,\xi)} = u + \frac{i\partial_u M_x^g(u,\xi)e^{i\Phi_x^g(u,\xi)}}{M_x^g(u,\xi)e^{i\Phi_x^g(u,\xi)}}$$
$$= u - \partial_\xi\Phi_x^g(u,\xi) + i\frac{\partial_\xi M_x^g(u,\xi)}{M_x^g(u,\xi)} \tag{65}$$

This demonstration has established the bridge between the center of gravity and the partial derivatives of the phase in a signal's time-frequency distribution. Moreover, the computation of two-dimensional integral in and can be transformed to the partial derivative of STFT, which reduce the computation complexity.

References

[1] L.F. Villa, A. Reñones, J.R. Perán, L.J. de Miguel, Statistical fault diagnosis based on vibration analysis for gear test-bench under non-stationary conditions of speed and load, Mech. Syst. Signal Process. 29 (2012) 436–446.
[2] G. Meltzer, Y.Y. Ivanov, Fault detection in gear drives with non-stationary rotational speed-part I: the time-frequency approach, Mech. Syst. Signal Process. 17 (2003) 1033–1047.
[3] S. Wang, G. Cai, Z. Zhu, W. Huang, X. Zhang, Transient signal analysis based on Levenberg–Marquardt method for fault feature extraction of rotating machines, Mech. Syst. Signal Process. 54–55 (2015) 16–40.
[4] R.B. Randall, Vibration-based diagnostics of gearboxes under variable speed and load conditions, Meccanica 51 (2016) 3227–3239.
[5] R. Yan, R.X. Gao, X. Chen, Wavelets for fault diagnosis of rotary machines: a review with applications, Signal Process. 96 (2014) 1–15.
[6] H. Cao, X. Zhang, X. Chen, The concept and progress of intelligent spindles: a review, Int. J. Mach. Tools Manuf. 112 (2017) 21–52.
[7] R. Zimroz, J. Urbanek, T. Barszcz, W. Bartelmus, F. Millioz, N. Martin, Measurement of instantaneous shaft speed by advanced vibration signal processing – application to wind turbine gearbox, Metrol. Meas. Syst. 18 (2011).
[8] I. Djurovi, L. Stankovi, An algorithm for the Wigner distribution based instantaneous frequency estimation in a high noise environment, Signal Process. (2004).
[9] F. Auger, P. Flandrin, Improving the readability of time-frequency and time-scale representations by the reassignment method, IEEE Trans. Signal Process. 43 (1995) 2038.

[10] F. Auger, P. Flandrin, Y. Lin, S. McLaughlin, S. Meignen, T. Oberlin, H. Wu, Time-frequency reassignment and synchrosqueezing: an overview, IEEE Signal Process. Mag. 30 (2013) 32–41.

[11] I. Daubechies, J. Lu, H. Wu, Synchrosqueezed wavelet transforms: an empirical mode decomposition-like tool, Appl. Comput. Harmon A 30 (2011) 243–261.

[12] N.E. Huang, Z. Shen, S.R. Long, M. Wu, H.H. Shih, Q.N. Zheng, N.C. Yen, C.C. Tung, H.H. Liu, The empirical mode decomposition and the Hilbert spectrum for nonlinear and non-stationary time series analysis, Proc. R. Soc. A-Math. Phys. 454 (1998) 903–995.

[13] G. Thakur, H.T. Wu, Synchrosqueezing-based recovery of instantaneous frequency from nonuniform samples, SIAM J. Math. Anal. (2012).

[14] G. Thakur, E. Brevdo, N.S. Fuckar, H. Wu, The Synchrosqueezing algorithm for time-varying spectral analysis: robustness properties and new paleoclimate applications, Signal Process. 93 (2013) 1079–1094.

[15] C. Li, M. Liang, Time–frequency signal analysis for gearbox fault diagnosis using a generalized synchrosqueezing transform, Mech. Syst. Signal Process. 26 (2012) 205–217.

[16] C. Li, M. Liang, A generalized synchrosqueezing transform for enhancing signal time–frequency representation, Signal Process. 92 (2012) 2264–2274.

[17] Z. Feng, X. Chen, M. Liang, Iterative generalized synchrosqueezing transform for fault diagnosis of wind turbine planetary gearbox under nonstationary conditions, Mech. Syst. Signal Process. 52–53 (2015) 360–375.

[18] S. Xi, H. Cao, X. Chen, X. Zhang, X. Jin, A frequency-shift synchrosqueezing method for instantaneous speed estimation of rotating machinery, J. Manuf. Sci. Eng.- Trans. ASME 137 (2015).

[19] S. Wang, X. Chen, G. Cai, B. Chen, X. Li, Z. He, Matching demodulation transform and synchrosqueezing in time-frequency analysis, IEEE Trans. Signal Process. 62 (2014) 69–84.

[20] S. Wang, X. Chen, C. Tong, Z. Zhao, Matching synchrosqueezing wavelet transform and application to aeroengine vibration monitoring, IEEE Trans. Instrum. Meas. 66 (2017) 360–372.

[21] S. Wang, X. Chen, I.W. Selesnick, Y. Guo, C. Tong, X. Zhang, Matching synchrosqueezing transform: a useful tool for characterizing signals with fast varying instantaneous frequency and application to machine fault diagnosis, Mech. Syst. Signal Process. 100 (2018) 242–288.

[22] H. Cao, S. Xi, X. Chen, S. Wang, Zoom synchrosqueezing transform and iterative demodulation: methods with application, Mech. Syst. Signal Process. 72–73 (2016) 695–711.

[23] S.T. Xi, H.R. Cao, X.F. Chen, Zoom synchrosqueezing transform for instantaneous speed estimation of high speed spindle, Mater. Sci. Forum (2016).

[24] N. Liu, J. Gao, X. Jiang, Z. Zhang, Q. Wang, Seismic time-frequency analysis via stft-based concentration of frequency and time, IEEE Geosci. Remote Sci. 14 (2017) 127–131.

[25] Z.L. Huang, J. Zhang, T.H. Zhao, Y. Sun, Synchrosqueezing S-transform and its application in seismic spectral decomposition, IEEE Trans. Geosci. Remote 54 (2016) 817–825.

[26] S.K. Guharay, G.S. Thakur, F.J. Goodman, S.L. Rosen, D. Houser, Analysis of non-stationary dynamics in the financial system, Econ. Lett. 121 (2013) 454–457.

[27] H. Wu, Y. Chan, Y. Lin, Y. Yeh, Using synchrosqueezing transform to discover breathing dynamics from ECG signals, Appl. Comput. Harmon A 36 (2014) 354–359.

[28] H. Wu, H. Wu, C. Wang, Y. Yang, W. Wu, T. Tsai, H. Chang, Modeling the pulse signal by wave-shape function and analyzing by synchrosqueezing transform, PLOS One 11 (2016) e157135.

[29] H. Wu, S. Hseu, M. Bien, Y.R. Kou, I. Daubechies, Evaluating physiological dynamics via synchrosqueezing: prediction of ventilator weaning, IEEE Trans. Bio-Med. Eng. 61 (2014) 736–744.

[30] Z. Wang, W. Ren, J. Liu, A synchrosqueezed wavelet transform enhanced by extended analytical mode decomposition method for dynamic signal reconstruction, J. Sound Vib. 332 (2013) 6016–6028.

[31] Y. Guo, X. Chen, S. Wang, X. Li, R. Liu, Fault diagnosis of wind turbine using local mean decomposition and synchrosqueezing transforms, in: 2016 IEEE International Instrumentation And Measurement Technology Conference Proceedings, 2016, pp. 1457–1462.

[32] J. Liu, Z. Wang, W. Ren, X. Li, Structural time-varying damage detection using synchrosqueezing wavelet transform, Smart Struct. Syst. 15 (2015) 119–133.

[33] M. Mihalec, J. Slavic, M. Boltezar, Synchrosqueezed wavelet transform for damping identification, Mech. Syst. Signal Process. 80 (2016) 324–334.

[34] L.A. Montejo, A.L. Vidot-Vega, Synchrosqueezed wavelet transform for frequency and damping identification from noisy signals, Smart Struct. Syst. 9 (2012) 441–459.

[35] H. Cao, Y. Yue, X. Chen, X. Zhang, Chatter detection in milling process based on synchrosqueezing transform of sound signals, Int. J. Adv. Manuf. Technol. (2016).

[36] H. Cao, Y. Yue, X. Chen, X. Zhang, Chatter detection based on synchrosqueezing transform and statistical indicators in milling process, Int. J. Adv. Manuf. Technol. (2017) 1–12.

[37] D. Pham, S. Meignen, High-order synchrosqueezing transform for multicomponent signals analysis—with an application to gravitational-wave signal, IEEE Trans. Signal Process. 65 (2017) 3168–3178.

[38] D.J. Nelson, Instantaneous higher order phase derivatives, Digit Signal Process. 12 (2002) 416–428.

[39] R.G. Baraniuk, P. Flandrin, A.J. Janssen, O.J. Michel, Measuring time-frequency information content using the Rényi entropies, IEEE Trans. Inf. Theory 47 (2001) 1391–1409.

[40] S. Aviyente, W.J. Williams, Minimum entropy time-frequency distributions, IEEE Signal Process. Lett. 12 (2005) 37–40.

[41] L. Cohen, Time-Frequency Analysis, Prentice Hall PTR, Englewood Cliffs, NJ, 1995.

[42] W. Sachse, Y.H. Pao, Time-frequency analysis of the dispersion of Lamb modes, J. Appl. Phys. 49 (1978) 4320–4327.

[43] H. Baid, C. Schaal, H. Samajder, A. Mal, Dispersion of Lamb waves in a honeycomb composite sandwich panel, Ultrasonics 56 (2015) 409–416.

[44] A. Giannoula, R.S. Cobbold, A. Bezerianos, Estimating the local viscoelastic properties from dispersive shear waves using time–frequency ridge analysis, Ultrasonics 53 (2013) 534–544.

[45] M. Niethammer, L.J. Jacobs, J.M. Qu, J. Jarzynski, Time-frequency representations of Lamb waves, J. Acoust. Soc. Am. 109 (2001) 1841–1847.

[46] W.H. Prosser, M.D. Seale, B.T. Smith, Time-frequency representation of Lamb waves using the reassigned spectrogram, J. Acoust. Soc. Am. 105 (1999) 2669–2676.

[47] R. Latif, M. Laaboubi, E.H. Aassif, G. Maze, Dispersion analysis of acoustic circumferential waves using time-frequency representations, Springer (2011) 183–205.

[48] C. Valle, J.W. Littles, Flaw localization using the reassigned spectrogram on laser-generated and detected Lamb modes, Ultrasonics 39 (2002) 535–542.

[49] Y. Yang, Z.K. Peng, W.M. Zhang, G. Meng, Z.Q. Lang, Dispersion analysis for broadband guided wave using generalized warblet transform, J. Sound Vib. 367 (2016) 22–36.

[50] M. Zhao, L. Zeng, J. Lin, W. Wu, Mode identification and extraction of broadband ultrasonic guided waves, Meas. Sci. Technol. 25 (2014).

[51] K. Xu, D. Ta, P. Moilanen, W. Wang, Mode separation of Lamb waves based on dispersion compensation method, J. Acoust. Soc. Am. 131 (2012) 2714–2722.

[52] K. Xu, D. Ta, W. Wang, Multiridge-based analysis for separating individual modes from multimodal guided wave signals in long bones, IEEE Trans. Ultrason. Ferr. 57 (2010) 2480–2490.

[53] H. Cao, L. Niu, S. Xi, X. Chen, Mechanical model development of rolling bearing-rotor systems: a review, Mech. Syst. Signal Process. 102 (2018) 37–58.

[54] Z.K. Peng, F.L. Chu, P.W. Tse, Detection of the rubbing-caused impacts for rotor-stator fault diagnosis using reassigned scalogram, Mech. Syst. Signal Process. 19 (2005) 391–409.

[55] H. Ma, T. Yu, Q. Han, Y. Zhang, B. Wen, X. Chen, Time-frequency features of two types of coupled rub-impact faults in rotor systems, J. Sound Vib. 321 (2009) 1109–1128.

[56] B. Chen, Z. Zhang, C. Sun, B. Li, Y. Zi, Z. He, Fault feature extraction of gearbox by using overcomplete rational dilation discrete wavelet transform on signals measured from vibration sensors, Mech. Syst. Signal Process. 33 (2012) 275–298.